Modulating RhoA effectors induces transitions to oscillatory and more wavelike RhoA dynamics in *Caenorhabditis elegans* zygotes

Baixue Yao[a,b], Seth Donoughe[a,c], Jonathan Michaux[d], and Edwin Munro[a,b,c,e,*]
[a]Department of Molecular Genetics and Cell Biology, [b]Committee on Cell Biology, [c]Committee on Development, Regeneration and Stem Cell Biology; and [e]Institute for Biophysical Dynamics, University of Chicago, Chicago, IL 60637; [d]Robotics Institute, University of Michigan, Ann Arbor, MI 48109

ABSTRACT **Pulsatile RhoA dynamics underlie a wide range of cell and tissue behaviors. The circuits that produce these dynamics in different cells share common architectures based on fast positive and delayed negative feedback through F-actin, but they can produce very different spatiotemporal patterns of RhoA activity. However, the underlying causes of this variation remain poorly understood. Here we asked how this variation could arise through modulation of actin network dynamics downstream of active RhoA in early *Caenorhabditis elegans* embryos. We find that perturbing two RhoA effectors—formin and anillin—induce transitions from nonrecurrent focal pulses to either large noisy oscillatory pulses (formin depletion) or noisy oscillatory waves (anillin depletion). In both cases these transitions could be explained by changes in local F-actin levels and depletion dynamics, leading to changes in spatial and temporal patterns of RhoA inhibition. However, the underlying mechanisms for F-actin depletion are distinct, with different dependencies on myosin II activity. Thus, modulating actomyosin network dynamics could shape the spatiotemporal dynamics of RhoA activity for different physiological or morphogenetic functions.**

Monitoring Editor
William Bement
University of Wisconsin, Madison

Received: Nov 2, 2021
Revised: Feb 1, 2022
Accepted: Feb 2, 2022

INTRODUCTION

Pulsatile dynamics underlie the physiological control of many different cellular behaviors including gene expression (Levine *et al.*, 2013), hormone secretion (Brabant *et al.*, 1992), neural and cardiac activity (DiFrancesco, 1993; Clay, 2005), cell migration (Arai *et al.*, 2010; Huang *et al.*, 2013), and tissue morphogenesis (Gorfinkiel *et al.*, 2009; Solon *et al.*, 2009; Rauzi *et al.*, 2010; Maître *et al.*, 2015; Sutherland and Lesko, 2020). The circuits that produce pulsatile dynamics are composed of different molecules, but they share a common architecture in which fast positive feedback drives an initial upswing in activity, and delayed negative feedback returns activity back toward basal levels (Meron, 1992). The pulses observed in different functional contexts vary widely in amplitude, duration, frequency, temporal regularity, and whether/how they propagate through space. How pulsatile dynamics arise in specific circuits and how they can be tuned to achieve different physiological outcomes remain poorly understood.

Here we focus on pulsatile dynamics of the small GTPase RhoA, which underlie intracellular remodeling, cell movement, shape change and division, epithelial tissue repair, and multicellular tissue morphogenesis (Ridley, 2015; Blanchard *et al.*, 2018; Sutherland and Lesko, 2020; Michaud *et al.*, 2021). Like other Rho family GTPases, RhoA binds to and diffuses within cellular membranes, where it transitions between inactive (GDP-bound) and active (GTP-bound) states. RhoA activation is governed by guanine nucleotide exchange factors (GEFs), while inactivation is governed by GTPase activating proteins (GAPs). The active form of RhoA binds to various downstream effectors, including formins, Rho kinase (ROK), and anillins, to control the assembly and contraction of cortical actomyosin networks.

Recent work has begun to identify the molecular mechanisms that govern positive and negative feedback on RhoA activity to produce pulsatile dynamics in different cell types. RhoA-dependent

This article was published online ahead of print in MBoC in Press (http://www.molbiolcell.org/cgi/doi/10.1091/mbc.E21-11-0542) on February 9, 2022.

*Address correspondence to: Edwin Munro (emunro@uchicago.edu).

Abbreviations used: FHN, Fitzhugh–Nagumo; GAP, GTPase activating protein; GEF, guanine nucleotide exchange factor; ROK, Rho kinase; tACF, temporal autocorrelation function.

accumulation or activation of RhoA GEFs is thought to provide the positive feedback that drives a rapid upswing in RhoA activity in activated frog and echinoderm eggs and embryos (Bement *et al.*, 2015), in U2OS cells (Graessl *et al.*, 2017), and in early *Caenorhabditis elegans* embryos (Nishikawa *et al.*, 2017; Michaux *et al.*, 2018). Stabilization of RhoA activity by its effector anillin (Budnar *et al.*, 2019), or concentration of active RhoA by myosin-dependent contractions (Munjal *et al.*, 2015), may also provide positive feedback in some cells. F–actin-dependent inhibition of RhoA provides delayed negative feedback that helps to terminate pulses of RhoA activity in frog and echinoderm embryos (Bement *et al.*, 2015), in early *C. elegans* embryos (Michaux *et al.*, 2018), and on secretory vesicles (Segal *et al.*, 2018). In *C. elegans* embryos and secretory vesicles, this inhibition is mediated by F–actin-dependent recruitment of specific RhoA GAPs, while in frog and echinoderm embryos, the molecules that mediate inhibition remain unknown. Overall, these studies suggest a potentially important role for actomyosin networks in shaping pulsatile RhoA dynamics.

The spatiotemporal patterns of pulsatile RhoA activity observed in different cells or tissues vary in terms of how pulses recur in time and whether/how they propagate through space. However, they can be classified into two main types: focal pulses, with variable frequency and regularity of recurrence and limited propagation, and oscillatory waves, which recur at regular intervals and propagate over longer distances. *Focal pulses* have been observed in cultured cells (Baird *et al.*, 2017; Graessl *et al.*, 2017), in early *C. elegans* embryos (Roh-Johnson *et al.*, 2012; Nishikawa *et al.*, 2017; Michaux *et al.*, 2018), *Drosophila* embryos and egg chambers (Gorfinkiel *et al.*, 2009; Rauzi *et al.*, 2010; Azevedo *et al.*, 2011), and at cell contacts in epithelial tissues (Reyes *et al.*, 2014; Stephenson *et al.*, 2019). *Oscillatory waves* have been observed in the eggs and early embryos of frogs and echinoderms (Bement *et al.*, 2015; Bhattacharya *et al.*, 2020), in mouse embryos during compaction (Maître *et al.*, 2015), and in tissue culture cells subjected to experimental perturbations (Murthy and Wadsworth, 2008; Xiong *et al.*, 2016; Michaud *et al.*, 2021). With one exception (Graessl *et al.*, 2017), focal pulses and oscillatory waves have not been observed in the same cells. Interestingly, artificial cortices prepared using extracts of frog egg cytoplasm can produce both locally oscillatory patches and single traveling waves of RhoA activity, suggesting the potential for a broader range of tunable variation in this system (Landino *et al.*, 2021). In general, the mechanistic basis for observed variations in pulsatile RhoA dynamics remains unknown.

Reaction diffusion models provide a useful framework for understanding how such variation could arise in simple activator/inhibitor systems (Allard and Mogilner, 2013). Depending on the relative strengths and timing of positive and negative feedback, the same circuit can exhibit *excitable dynamics*, in which a local perturbation, whose amplitude exceeds some threshold, is required to drive the system away from a stable rest state to induce a single pulse of activity, followed by a return to the rest state, or *oscillatory dynamics*, in which pulses recur with a fixed frequency in the absence of external perturbations (Strogatz, 2019). Similarly, the same circuit can generate *focal pulses* (also known as standing pulses) when the inhibitor diffuses faster than the activator (Hecht *et al.*, 2010), or *traveling pulses*, when the activator diffuses faster than the inhibitor (Koga and Kuramoto, 1980; Ermentrout *et al.*, 1984; Klaasen and Troy, 1984; Dockery and Keener, 1989). Thus in principle, the range of variation in RhoA pulse dynamics observed in different contexts could be explained by differences in the relative strength/timing of activation and inhibition and/or the relative mobilities of activators and inhibitors.

However, efforts to use such simple models to explain pulsatile RhoA dynamics observed in vivo highlight a basic puzzle: echinoderm, frog, and nematode cells appear to use the same basic circuit architecture combining fast autoactivation of RhoA with delayed negative feedback via local F-actin assembly (Figure 1A). Simple reaction diffusion models, treating RhoA as a fast-diffusing activator and F-actin (and associated GAPs) as a slow-diffusing inhibitor, recapitulate the *oscillatory waves* of RhoA activity observed in frog and echinoderm cells (Bement *et al.*, 2015) but not the focal pulses observed in nematodes. Thus the focal pulses observed in nematodes must involve additional forms of feedback and/or through different mechanisms of coupling RhoA activity to the dynamics of actomyosin assembly and contractility. However, incomplete knowledge of circuit components, difficulties in measuring the strength and timing of positive and negative feedback, and differences in actomyosin network architecture and assembly dynamics make it challenging to determine the origins of pattern variation by comparisons across different cell types.

Here we take an alternative approach, using the one-cell *C. elegans* embryo as a model system to ask: is it possible to reproduce the pattern variants observed across different cell types in a single cell by modulating actomyosin dynamics downstream of RhoA? We perturbed proteins that regulate actomyosin architecture, assembly dynamics, and contractility; developed new computational tools to quantify the local recurrence and spread of RhoA activity; and looked for perturbations that induce shifts from excitable to oscillatory dynamics and from focal to traveling pulses.

We identified perturbations to two different RhoA effectors—formin and anillin—that induce an apparent shift from excitable to oscillatory dynamics. Both conditions also induce increased spread of RhoA activity but with qualitatively different spatial patterns: formin depletion produces larger, but still spatially delimited, focal pulses, Anillin depletion produces a noisy version of the oscillatory waves observed in other systems, in which pulses spread locally and continuously, frequently merging and splitting, to explore large regions of the cell cortex. For both perturbations, the increase in local recurrence and the spread of pulsatile RhoA activity are accompanied by a decrease in overall F-actin levels and enhanced local F-actin depletion that is tightly synchronized with local pulse initiation. However, the transition to large recurrent focal pulses produced by inhibiting formin requires actomyosin contractility and is associated with local contractile instabilities, while the transition to noisy oscillatory waves produced by anillin depletion is independent of contractility. These results provide new insight into how the modulation of actomyosin network assembly and contractility could shape pulsatile RhoA dynamics to achieve different physiological or morphogenetic outcomes.

RESULTS

Modulating actomyosin dynamics can induce shifts in both spatial and temporal pulse dynamics

During polarization of *C. elegans* zygotes, focal pulses of RhoA activity and actomyosin contractility are superimposed on long-range cortical flows, which are induced by a posterior centrosomal cue (Cowan and Hyman, 2004; Munro *et al.*, 2004; Mayer *et al.*, 2010). These flows progressively segregate actomyosin, polarity factors, and RhoA activity toward the future anterior pole (Munro *et al.*, 2004; Motegi and Sugimoto, 2006; Dickinson *et al.*, 2017; Rodriguez *et al.*, 2017); thus they introduce an additional level of spatial and temporal variation in RhoA pulse dynamics. To focus on local changes in pulse dynamics without the confounding effects of long-range flows (Nishikawa *et al.*, 2017), we perturbed actomyosin

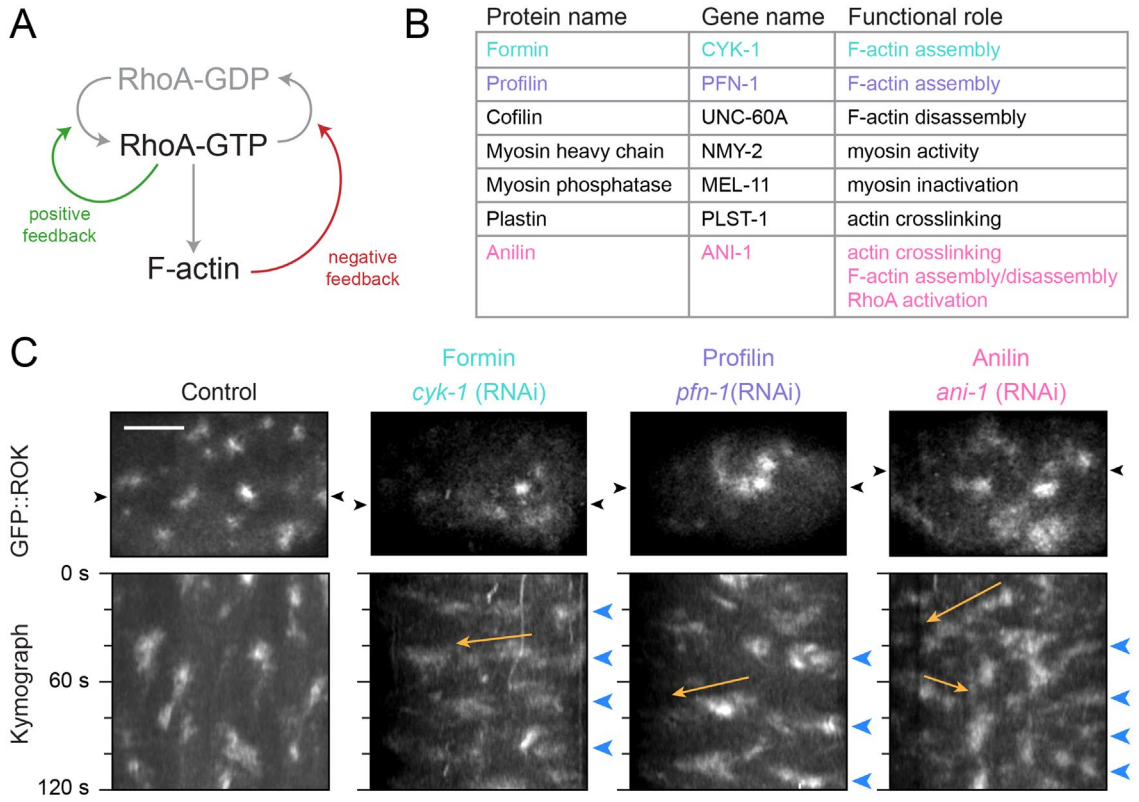

FIGURE 1: Modulating actomyosin dynamics generates qualitatively distinct patterns of RhoA activation. (A) Schematic representation of the molecular circuit for RhoA pulse dynamics. (B) Regulators of actomyosin dynamics that were perturbed in this study. (C) Single frames (top) and kymographs (bottom) showing patterns of ROK distribution in control, *cyk-1(RNAi),* and *ani-1(RNAi)* embryos. Fluorescence intensity is scaled differently across phenotypes to highlight variations in ROK distribution. Black arrowheads indicate the vertical position where the kymograph is generated. Blue arrowheads indicate recurrence of ROK accumulation at regular intervals. Orange lines and arrows indicate diagonally oriented streaks. Scale bar is 10 μm.

dynamics in embryos depleted of the centrosomal scaffold protein SPD-5 (Hamill *et al.*, 2002), which lack functional centrosomes.

We began by looking for perturbations to cortical actin assembly, disassembly, architecture, and contractility that induce changes in the frequency and regularity of local excitation or in the spatial spread of excitation (Figure 1B). We used endogenously tagged ROK (GFP::LET-502, hereafter GFP::ROK) as a reporter for RhoA activity (Piekny *et al.*, 2003; Maddox *et al.*, 2007; Bell *et al.*, 2020). We reduced F-actin assembly by depleting formin/CYK-1 or its cofactor profilin/PFN-1 (Neidt *et al.*, 2008, 2009), and we reduced F-actin disassembly by depleting cofilin/UNC-60A (Ono *et al.*, 2003). We used a temperature-sensitive mutation in the nonmuscle myosin II heavy chain NMY-2 [nmy-2(ts); Liu *et al.*, 2010] to sample reduced contractility and we enhanced contractility by depleting the myosin phosphatase/MEL-11 (Piekny *et al.*, 2003). We used embryos mutant for the cross-linker plastin/PLST-1 [*plst-1(tm2455)*] to sample reduced network connectivity (Ding *et al.*, 2017). We also depleted the scaffolding protein anillin/ANI-1 (Maddox *et al.*, 2005, 2007; Piekny and Glotzer, 2008; Tse *et al.*, 2011), which cross-links actin filaments and is also reported to affect actin turnover (Tian *et al.*, 2015), myosin dynamics (Pacquelet *et al.*, 2015), and RhoA activity (Budnar *et al.*, 2019).

We used time-lapse analysis and kymography to assess qualitative changes in pulsatile RhoA dynamics in response to these different perturbations (Figure 1C; Supplemental Figure S1, A and B; Supplemental Movies S1–S3; see *Methods*). We observed three general classes of spatiotemporal patterns. First, in control embryos, GFP::ROK appeared as small transient focal pulses with no obvious pattern of recurrence (Figure 1C), as previously observed with a different RhoA biosensor (Michaux *et al.*, 2018). The general pattern of nonrecurrent focal pulses was also observed in embryos with reduced or enhanced contractility [*nmy-2(ts)* and *mel-11(RNAi)*, respectively], or in embryos with reduced cross-linking by PLST-1 [*plst-1(tm2455)*] (Supplemental Figure S1A; Supplemental Movie S2). Second, cofilin depletion induced a higher density of focal pulses, and these recurred with higher frequency, producing long vertical streaks of GFP::ROK with fluctuating intensities in kymographs (Supplemental Figure S1B; Supplemental Movie S3). Finally, three perturbations [*ani-1(RNAi)*, *cyk-1(RNAi)* and weak *pfn-1(RNAi)*] induced shifts toward higher frequency, more regular recurrence, and larger domains of RhoA activity, consistent with a shift toward oscillatory dynamics and increased spread of RhoA activity (Figure 1C). In *ani-1(RNAi)* embryos, pulses of GFP::ROK accumulation often appeared to propagate locally at approximately constant speeds; this could be readily seen in time-lapse movies (Supplemental Movie S1) and as diagonal streaks of GFP::ROK in kymographs (orange arrows in Figure 1C). In *cyk-1(RNAi)* or *pfn-1(RNAi)* embryos, pulsed accumulations of GFP::ROK are synchronized across larger regions producing wide, nearly horizontal streaks in kymographs (orange arrows in Figure 1C). In summary, multiple ways of perturbing actomyosin dynamics lead to increased frequency and regularity and greater spread of RhoA excitation, consistent with a shift toward oscillatory and wavelike RhoA dynamics. We therefore focused on analyzing the

differences in spatiotemporal dynamics produced by these perturbations.

A computational pipeline to identify regions undergoing RhoA excitation

To quantify and compare spatiotemporal patterns of RhoA activity across different perturbations, we developed computational methods to automate the detection of regions undergoing the initiation of RhoA pulses, which we will refer to here as RhoA excitation (see *Methods* for details). We based our approach on a simple observation: for each perturbation in manually chosen pulsing regions, after smoothing the raw data (Figure 2A: [1] and [2]), we could detect the sharp rising phase of RhoA excitation at individual pixels (Figure 2B). To automate detection of the rising phase, we computed the temporal derivative of the smoothed data divided by its standard deviation to normalize (Figure 2A: [3]) and then applied a threshold to produce binary masks representing all pixels currently undergoing excitation (Figure 2C). From these binary masks, we identified *excitation regions* as contiguous groups of pixels undergoing excitation (i.e., with temporal derivatives above threshold) (Figure 2A: [4]) and *new excitation regions* as groups of pixels crossing the excitation threshold for the first time (Figure 2A: [5]).

To account for genotype-specific variations in the amplitude of the temporal derivative of GFP::ROK, we set the excitation threshold for each genotype as follows: we computed the average amplitude of the temporal derivative across many manually labeled pulsing regions. Then we multiplied by a single scale factor S = 0.4, shared across all perturbations, to obtain a perturbation-specific threshold value (Figure 2D). Overlaying new excitation regions on the raw GFP::ROK signal shows that, for a single choice of scale factor, our algorithm accurately captures pulses for three different perturbations (Figure 2E). These and the results of our subsequent analysis of spatiotemporal excitation dynamics were largely insensitive to variation in the magnitude of the scale factor up or down by 10% (Supplemental Figure S2).

Depleting formin/CYK-1 or anillin/ANI-1 induces a shift from locally excitable to noisy oscillatory dynamics

To characterize changes in temporal dynamics induced by formin and anillin depletion, we analyzed the recurrence of excitation at individual pixels. Comparing embryowide frequency maps (Figure 3A) and kymographs of new excitation events (Figure 3B) revealed an increase in both the frequency and the regularity of new excitation in *cyk-1(RNAi)* and *ani-1(RNAi)* embryos compared with controls. To quantify these differences, we plotted distributions of new excitation frequency and wait times between new excitations for control, *cyk-1(RNAi)*, and *ani-1(RNAi)* embryos (Figure 3, C and D). In control embryos, the distribution of frequencies was highly skewed, with a peak near 0, and the distribution of wait times was approximately uniform with a refractory period near 0 (Figure 3, C and D; Supplemental Figure S2B). By contrast, in *cyk-1(RNAi)* or *ani-1(RNAi)* embryos, the distribution of frequencies was nearly symmetric with peaks near 0.04/s, while the distribution of wait times was unimodal with strong peaks near 23 s (Figure 3, C and D; Supplemental Figure S2B). For all three phenotypes, there was a slight peak in the wait time distribution at around 10 s which likely reflects small cortical displacements that we do not account for in this analysis. We also measured the average temporal autocorrelation function (tACF) of smoothed GFP::ROK intensities (see *Methods*) in control, *cyk-1(RNAi)*, and *ani-1(RNAi)* embryos. In control embryos, the tACF was monotonically decreasing, while in *cyk-1(RNAi)* and *ani-1(RNAi)* embryos, the tACF had a small secondary peak at around 23 s (Supplemental Figure S3), confirming that pulses of RhoA excitation become more regular on depletion of formin or anillin.

To help interpret these differences, we compared the experimental distributions with those produced by simulations of the Fitzhugh–Nagumo (FHN) model (Nagumo *et al.*, 1962), a generic model of an excitable system subjected to stochastic input (Supplemental Figure S4A; see *Methods* for details). We held the amplitude and frequency of the stochastic input fixed and gradually reduced the value of a single parameter (α) so that the deterministic behavior of the FHN model transitions from excitable to oscillatory (Supplemental Figure S4B). When α was tuned to yield excitable dynamics with a large threshold relative to the amplitude of the stochastic input, the FN model predicted frequency and wait time distributions that were qualitatively similar to those observed in controls (Supplemental Figure S4, C and D; $\alpha = 0.95$). As α increased, the excitation threshold decreased; the frequency distribution shifted right and became more symmetric, and a peak appeared in the wait time distribution (Supplemental Figure S4, C and D; $\alpha = 0.9$). As α approached the bifurcation point at which the deterministic dynamics switched from excitable to oscillatory, the peak in the frequency distribution approached the frequency of the oscillation and the wait time distribution tightened around its natural period. As α passed through this bifurcation point, qualitative features of the distributions of frequency and wait time were preserved (Supplemental Figure S4, C and D; $\alpha = 0.85, 0.65$). Thus in the presence of fixed stochastic input, when the system is close to a transition from excitable to oscillatory dynamics, it is not possible to infer from the observed dynamics alone whether the underlying deterministic system is excitable or oscillatory. We will use the term *noisy oscillations* to describe this type of observed dynamics. Comparing predictions of the FHN model with stochastic forcing with the frequency and wait time distributions measured in *cyk-1(RNAi)* and *ani-1(RNAi)* embryos suggests that depleting either *cyk-1*/CYK-1 or anillin/ANI-1 induces a transition from excitable RhoA dynamics to noisy oscillatory dynamics.

Depleting formin and anillin induces different spatiotemporal patterns of excitation

To visualize and compare the spread of RhoA excitation across different perturbations, we assigned grayscale values to excitation pixels based on the time since last excitation. The resulting movies (Supplemental Movie S4) show that local spread of new excitation occurs across all perturbations. but the patterns of spread are markedly different in *cyk-1(RNAi)* or *ani-1(RNAi)* embryos than in controls. In control embryos, excitations tend to initiate and spread locally before terminating. In formin- and anillin-depleted embryos, regions of locally spreading excitation cover a larger fraction of the cortex and frequently merge with one another or split to form more complicated spatial patterns of excitation.

To quantify these differences, we first measured the speeds at which the boundaries of excitation regions (excitation fronts) advance locally between successive frames (Figure 4A; see *Methods* for details). If the dominant mode of propagation were coherent excitation wavefronts as observed in other cells (Bement *et al.*, 2015; Maître *et al.*, 2015; Bhattacharya *et al.*, 2020), the distribution of speeds would have a single dominant peak centered on a nonzero value. Instead, the distributions that we observe in *C. elegans* zygotes are monotonically decreasing with a peak near zero velocity and long tails (Figure 4B). However, the distributions of speeds were remarkably similar in control, *ani-1(RNAi)*, and *cyk-1(RNAi)* embryos, suggesting that differences in the speeds at which excitation spreads

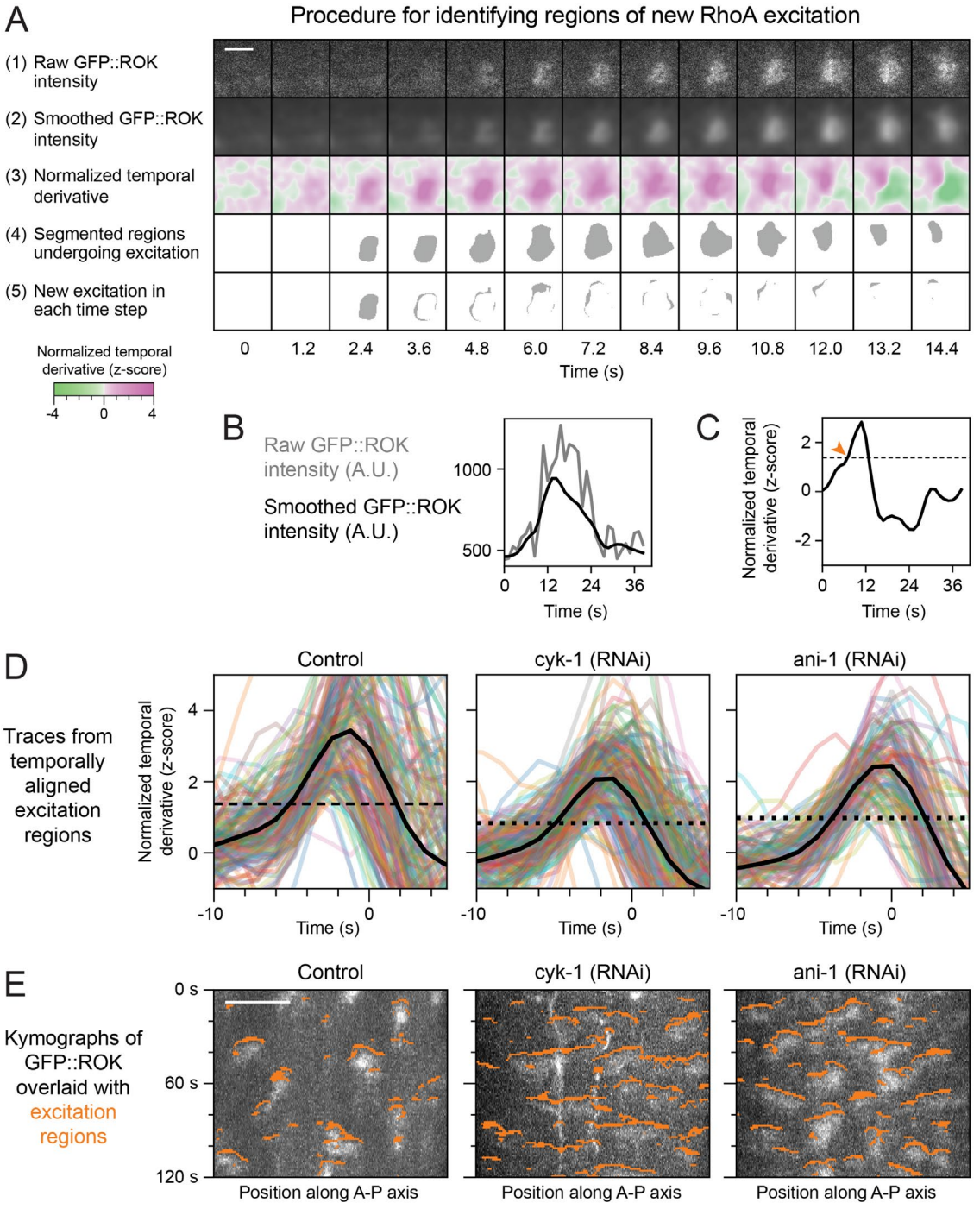

FIGURE 2: A pipeline for automated detection of RhoA excitation. (A) Time evolution of a single pulse illustrating image processing steps that convert the raw GFP::ROK signal into binary masks representing RhoA excitation. Top row: raw GFP::ROK intensity. Second row: smoothed signal obtained by averaging raw signal in space and time (see *Methods*). Third row: normalized temporal derivative calculated by subtracting the smoothed signal at $t - 2.4$ s from the smoothed signal at $t + 2.4$ s and then dividing by its standard deviation. Fourth row: binary excitation mask obtained by thresholding the normalized temporal derivative (see panel C). Bottom row: binary subtraction of excitation in previous frame from current frame yields new excitation. The time delay between frames is 1.2 s. The selected region is 7 μm square. (B) Time evolution of the raw and smoothed intensities for the center pixel of the region in A. The gray line indicates the raw GFP::ROK signal; the black line indicates the smoothed signal. (C) Time evolution of normalized temporal derivative values for the center pixel in A. The black line indicates the normalized temporal derivative; the dotted black line indicates the threshold used in A; the orange arrowhead indicates the new excitation time point. (D) Time evolution of the normalized temporal derivative value of ROK over time. The thin colored lines show the normalized temporal derivative for pixels within many manually labeled regions in embryos subjected to the indicated perturbation. The thick black line is their average. The dotted black line is the selected threshold for all embryos subjected to the indicated perturbation. (E) Kymographs showing new excitation in orange superimposed on the raw GFP::ROK intensities for the indicated perturbations. Scale bar is 10 μm.

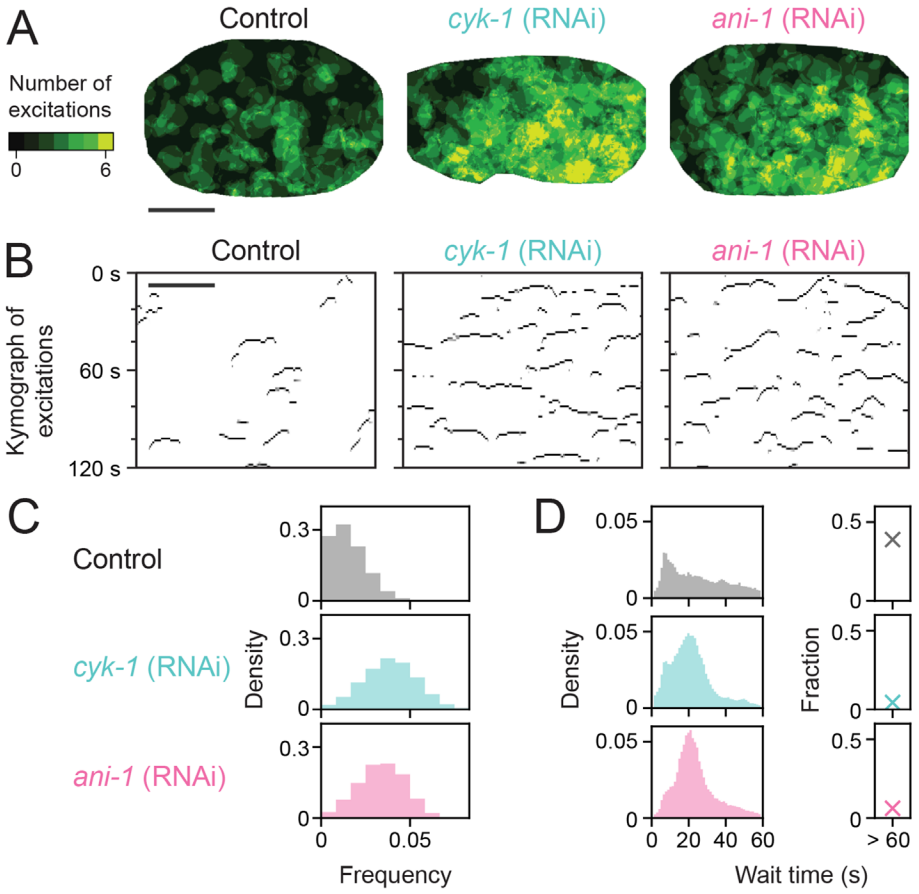

FIGURE 3: Depletion of CYK-1 or ANI-1 induces a shift from locally excitable to noisy oscillatory RhoA dynamics. (A) Colormaps showing the total number of excitations in 120 s for each pixel in representative control, *cyk-1(RNAi)* and *ani-1(RNAi)* embryos. The number of excitations is color coded using the colorbar on the left. (B) Kymograph showing new excitation events (black) over time for the center row of pixels in A. (C) Distributions of excitation frequencies for all pixels in embryos with the indicated perturbations. Frequency is the total number of excitations divided by 120 s. The dotted line is the best Poisson fit. (D) Distributions of wait times between new excitations for all new excitation events in embryos with the indicated perturbations. On the right is the fraction of pixels at which new excitation did not recur within 60 s. The numbers of embryos used for the analysis in C and D are control/*spd-5(RNAi)* ($n = 6$). *spd-5(RNAi)*; *cyk-1(RNAi)* ($n = 8$) and *spd-5(RNAi)*; *ani-1(RNAi)* ($n = 5$). The total numbers of excitation events examined are control/*spd-5(RNAi)* ($n = 615914$), *spd-5(RNAi)*; *cyk-1(RNAi)* ($n = 561054$), and for all cyk-1(RNAi) embryos and *spd-5(RNAi)*; *ani-1(RNAi)* ($n = 349737$). Scale bar is 10 μm.

locally are not responsible for larger differences in spatiotemporal patterns of excitation.

To characterize differences in spatiotemporal patterns of excitation, we linked excitation regions that overlap in successive frames (Figure 4D; see *Methods* for details). We applied this linkage recursively over the entire observation window to identify a set of "linked excitation regions" connecting excitation regions that spread locally, merge with one another or split over time (Figure 4, C and D). Visualizing and quantifying the cumulative growth, duration, and distribution of linked excitation regions in representative control, *cyk-1(RNAi)*, and *ani-1(RNAi)* embryos revealed different patterns of spreading excitation (Supplemental Movie S5; Figure 4, E and F). In control embryos, linked excitation regions have small cumulative areas and durations (Figure 4, E and F), reflecting the tendency for excitations to initiate locally, expand rapidly and then terminate quickly without merging or splitting (Supplemental Movie S5). We also observe linked excitation regions with small areas and short durations in formin- and anillin-depleted embryos, but in these embryos, the frequent merging and splitting of excitation regions also generate a few linked excitation regions that persist longer and cover much of the embryo surface. We confirmed these basic differences by plotting the durations and cumulative areas of the largest linked excitation regions for multiple embryos with each perturbation (Figure 4, G and H; Supplemental Figure S2C).

Closer inspection suggested that differences in the spatial synchronization of excitation produces different spatiotemporal patterns of excitation in formin- and anillin-depleted embryos (Figure 4, G and H; Supplemental Movie S5). In formin-depleted embryos, the larger linked excitation groups represent multiple excitation regions that initiate synchronously and then rapidly expand and merge into larger regions before terminating (Supplemental Movie S5). Multiple rounds of synchronous excitation recur at intervals comparable to the mean wait time for excitation (Figure 4E) and in overlapping regions of the embryo (Figure 4F). In anillin-depleted embryos, new excitation regions initiate throughout the cortex without apparent synchrony. They often form adjacent to existing or recent excitation regions and frequently merge with one another or split, giving the overall impression of noisy waves that expand locally and persistently in different directions, colliding with one another to create larger linked excitation regions that span most of the embryo (Figure 4, E and F; Supplemental Movie S5).

In summary, depleting either formin/CYK-1 or anillin/ANI-1 has only minor effects on the distribution of speeds at which excitation spreads locally but large effects on spatiotemporal patterns of RhoA excitation. In control embryos, many excitations initiate and spread locally and terminate rapidly. In formin-depleted embryos, recurrent episodes of excitation are synchronized over larger regions of the cortex. In anillin-depleted embryos, excitations initiate asynchronously, spread locally, and frequently merge and split to explore larger regions of the cell cortex.

Lower levels and enhanced depletion of F-actin underlie the shift in spatiotemporal patterns of RhoA excitation in formin- and anillin-depleted embryos

Our data suggest that depleting either formin or anillin induces a transition from locally excitable to noisy oscillatory dynamics. In simple activator/inhibitor models, such transitions can be induced by reducing overall inhibitor levels and/or by enhancing the depletion of inhibitor after individual pulses. Consistent with the first possibility, we observed an overall reduction in F-actin levels in both anillin- and formin-depleted embryos relative to controls [Figure 5A, control: 440 ± 29; *ani-1(RNAi)*: 403 ± 23; *cyk-1(RNAi)*: 350 ± 6 (mean ± SD in arbitrary units of intensity)].

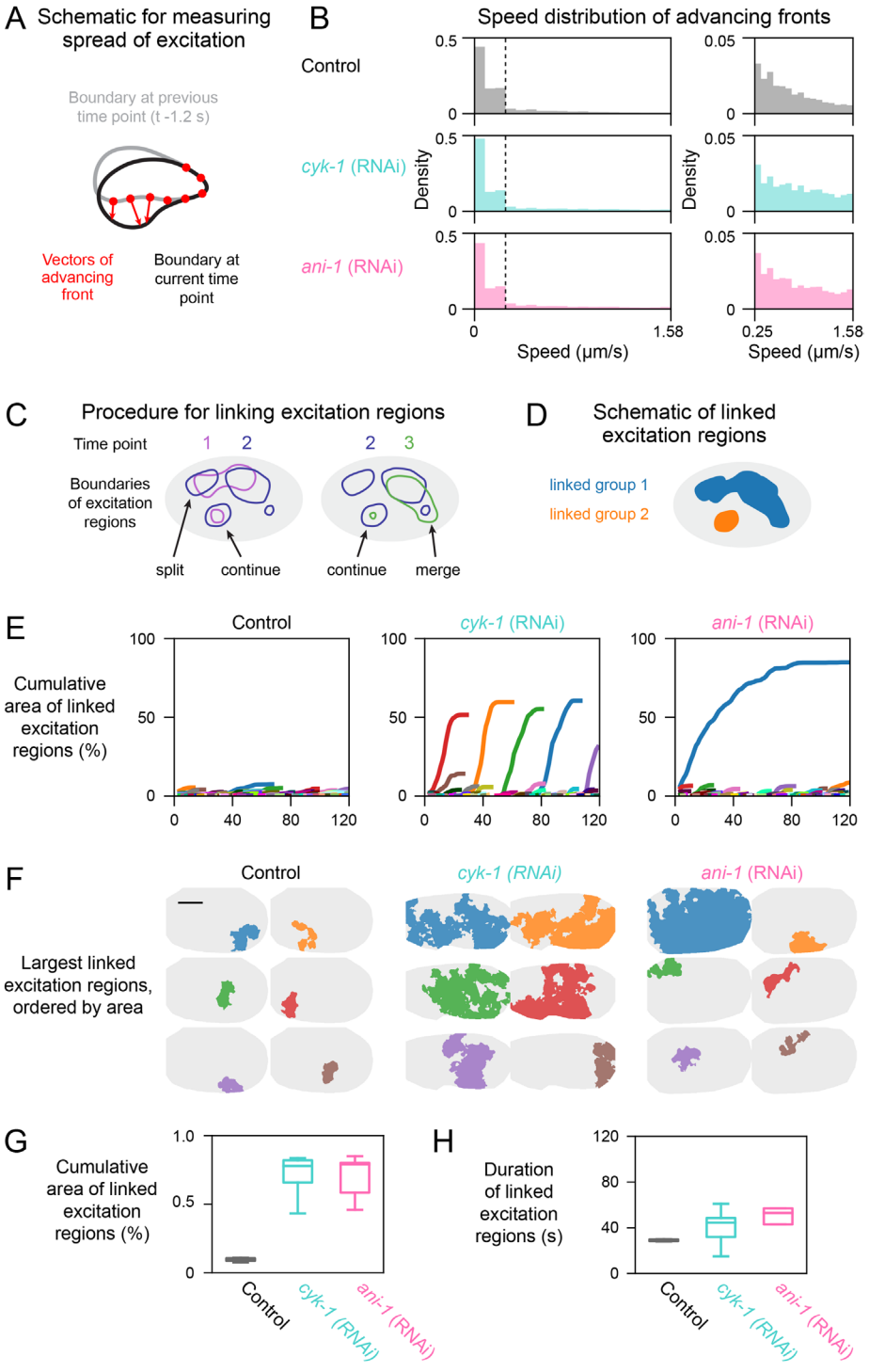

FIGURE 4: Depletion of CYK-1 and ANI-1 induce distinct spatiotemporal patterns of RhoA excitation. (A) Schematic showing the method for quantifying local spread of excitation. Black and gray lines are the boundaries of excitation regions at times *t* and *t* – 1.2 s, respectively. Red dots are equally spaced points along the part of the excitation front at time t that advanced by time *t* – 1.2. Red arrows show displacement normal to the local excitation front at time *t*. (B) Distribution of local speeds in embryos of the indicated perturbation. Magnified view at the right shows the tail of the distributions for speeds >0.25 μm/s shown as black dotted line at the left. (C) Schematic illustration of linking excitation regions across successive frames. Closed lines show the contours of excitation regions. Line colors indicate successive time points. Left shows examples of splitting and continuation between time points 1 and 2. Right shows examples of continuation and merger between time points 2 and 3. (D) Schematic illustration of linked excitation regions corresponding to the linkage sequences in C. (E) Curves showing the growth of cumulative area vs. time for all linked excitation region in representative embryos for the indicated perturbation. Each colored line indicates the growth of a single linked excitation regions over time. (F) Areas explored by the six largest excitation regions for each representative embryo. Colors correspond to the lines in E. The "representative" embryos in E and F were chosen to best highlight qualitative differences across perturbations. (G) Box plots showing the distribution of cumulative areas of the largest linked excitation regions in embryos with the indicated perturbations. (H) Box plots showing the duration of the largest linked excitation regions in embryos with the indicated perturbations. The numbers of embryos used for the analysis in G&H are control/*spd-5(RNAi)* ($n = 6$). *spd-5(RNAi); cyk-1(RNAi)* ($n = 8$) and *spd-5(RNAi); ani-1(RNAi)* ($n = 5$). The numbers of vectors at advancing fronts in B are control/*spd-5(RNAi)* ($n = 45496$), *spd-5(RNAi); cyk-1(RNAi)* ($n = 82638$), and for all cyk-1(RNAi) embryos and *spd-5(RNAi); ani-1(RNAi)* ($n = 47574$).

To assess whether enhanced depletion of F-actin after pulses accompanies the transition to noisy oscillatory dynamics in formin- and anillin-depleted embryos, we imaged embryos coexpressing ROK::GFP and Lifeact::mCherry as a marker for F-actin (Pohl *et al.*, 2012). As above, we used the GFP::ROK signal to identify pixels undergoing new excitation and then used kymographs and movies to compare new excitation with F-actin levels (Supplemental Figure S5A) or their temporal derivatives (Figure 5B; Supplemental Figure S2D; Supplemental Movie S6) in space and time. In formin- and anillin-depleted embryos, local depletion of F-actin occurs shortly before the majority of RhoA excitations (and the majority of excitations follow shortly after F-actin depletion). In control embryos, the relationship between F-actin depletion and RhoA excitation was more variable; some excitations follow F-actin depletion; others do not (Figure 5B; Supplemental Figure S5A; Supplemental Movie S6). To quantify the strength of temporal correlations between F-actin depletion and RhoA excitation under different perturbations, we measured the average Lifeact::mCherry intensity (Supplemental Figures S5C and S2D), and its temporal derivative (Figure 5C) in excitation pixels at a range of temporal offsets relative to new excitation. We found that on average, Lifeact::mCherry intensities decreased sharply just before new excitation in *cyk-1(RNAi)* and *ani-1(RNAi)* embryos but not in control embryos (Figure 5C; Supplemental Figure S5C, discussed further below). Thus overall reduction in levels and

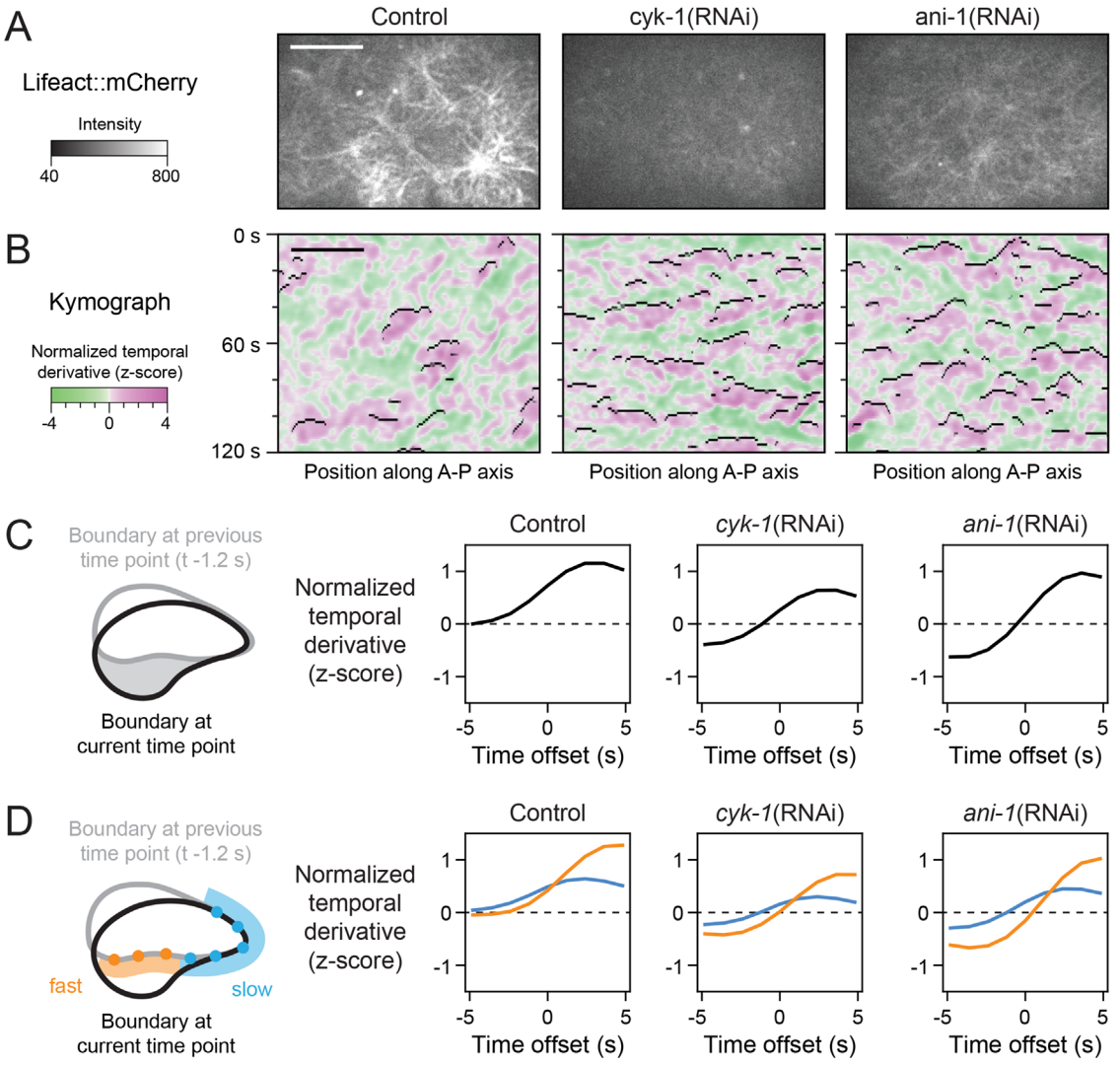

FIGURE 5: Reduced levels and more rapid depletion of F-actin accompanies the transition to noisy oscillatory dynamics in formin- and anillin-depleted embryos. (A) Single spinning disk images of embryos expressing mCherry::Lifeact. Images were acquired with identical settings and identically processed to allow direct comparison of intensities across perturbations. (B) Kymographs showing the normalized temporal derivative of mCherry::Lifeact intensity, calculated as shown in Figure 2A, for the vertically centered row of pixels from the embryos in A, overlaid with new excitation pixels in black, which were calculated as in Figure 2A. (C) Left: schematic showing new excitation region at time *t* in solid gray. Right: average normalized temporal derivative of mCherry::Lifeact intensity measured over all new excitation pixels in embryos with the indicated perturbations. (D) Left: schematic representation of pixels evenly spaced along the advancing boundary of an excitation front, color coded with respect to the instantaneous speed of advance; orange indicates large instantaneous speed ($S >= 0.25$ μm/s); blue indicates small instantaneous speed ($S < 0.25$ μm/s). Right: average normalized temporal derivative of mCherry::Lifeact intensity measured over all new excitation pixels with fast (orange) or slow (blue) instantaneous speeds in embryos with the indicated perturbations. (C, D) The 95% confidence intervals for average F-actin level are smaller than the thickness of the average line. the dotted black line indicates a temporal derivative = zero; that is, no change in F-actin level. The numbers of embryos used for the analysis in C and D are control/*spd-5(RNAi)* ($n = 6$). *spd-5(RNAi); cyk-1(RNAi)* ($n = 8$) and *spd-5(RNAi); ani-1(RNAi)* ($n = 5$). The total numbers of excitation events examined are control/*spd-5(RNAi)* ($n = 615914$), *spd-5(RNAi); cyk-1(RNAi)* ($n = 561054$), and for all cyk-1(RNAi) embryos and *spd-5(RNAi); ani-1(RNAi)* ($n = 349737$). Scale bar is 10 μm.

enhanced local depletion of F-actin accompanies the shift to noisy oscillatory dynamics in both formin- and anillin-depleted embryos.

To ask whether local spread of excitation correlates with local depletion of F-actin in formin- and anillin-depleted embryos, at each time point we partitioned pixels along the advancing boundaries of excitation regions ("excitation fronts") into fast and slow groups based on the speed of local advance. For each pixel, we measured Lifeact::mCherry intensity or its temporal derivative in regions just ahead of the excitation front (see Figure 5D schematic: orange and blue regions) at different times relative to the current time point (Figure 5D; Supplemental Figure S5D; see *Methods*). In formin- and anillin-depleted embryos, the average F-actin levels decreased in regions ahead of excitation fronts shortly before the time of entry (Figure 5D; Supplemental Figures S5D and S2D; note that slow-moving excitation fronts enter but do not spread through these regions). The average rate and

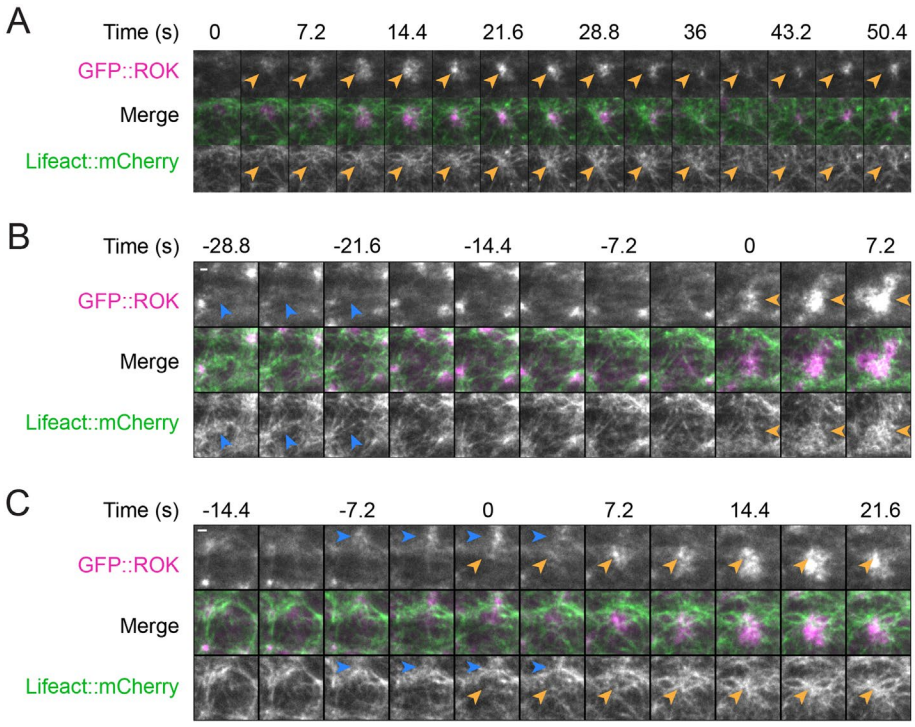

FIGURE 6: Heterogeneous dynamics of pulse initiation and spread in control embryos. Time series of TIRF images from Supplemental Movie S7 showing examples of pulse initiation and spread in a control embryo expressing GFP::ROK and mCherry::Lifeact. Time zero indicates initiation of pulses. (A) A GFP::ROK focus forms from a larger pulse and then persists in a region with high levels of mCherry::Lifeact (orange arrowheads). (B) Local cortical tearing and dilation (blue arrowheads) creates a region with reduced F-actin levels where a new pulse initiates (orange arrowheads). (C) A new pulse initiates near an existing GFP::ROK focus (blue arrowheads) and then spreads into a region with lower levels of mCherry::Lifeact (orange arrowheads). Scale bar is 10 μm.

extent of decrease were lower ahead of slowly advancing excitation fronts than faster moving ones (Figure 5D; Supplemental Figures S5D and S2D). In control embryos, there was a slight decrease in average F-actin levels in regions ahead of fast advancing excitation fronts but none ahead of slowly advancing fronts. These observations suggest that local depletion of F-actin plays a role in channeling the spread of RhoA excitation in formin- and anillin-depleted embryos.

Heterogeneous F-actin dynamics precede RhoA excitation in control embryos

We have shown that, on average, local depletion of F-actin does not precede RhoA excitation in control embryos. However, this does not rule out a role for F-actin inhibition in control embryos because these average measurements hide significant heterogeneity in the local F-actin dynamics preceding RhoA excitation (Figure 5B; Supplemental Figure S5B; Supplemental Movie S6). To better understand the origins of this heterogeneity, we used near-TIRF microscopy (see *Methods*) to image control embryos expressing GFP::ROK and Lifeact::mCherry (Figure 6; Supplemental Movie S7). In control embryos, as previously described (Munro *et al.*, 2004), the cortex contains a dynamic network of actin foci interconnected by bundles that surround "depletion regions" with relatively lower levels of F-actin. The foci are coenriched in F-actin and GFP::ROK. They typically form as condensations of larger RhoA pulses, and they often persist for tens of seconds and propagate slowly through regions with high levels of F-actin (Figure 6A; see also Michaux *et al*, 2018), suggesting that additional mechanisms may exist to sustain and/or propagate RhoA activity in regions with high levels of F-actin.

We observed that new RhoA pulses tend to form and spread within F-actin depletion regions. But where excitation first initiates within these regions is more variable. Pulses can initiate within the interiors of depletion regions where F-actin levels are relatively low, and this is sometimes (<10% of pulses) preceded by spontaneous local tearing and dilation of the cortical network (Figure 6B). However, pulses often initiate near the boundaries of depletion regions, and near existing foci where F-actin levels are persistently high and/or increasing (Figure 6C). These observations suggest that local depletion of F-actin helps to shape, but does not determine, patterns of RhoA excitation in control embryos.

Contractility is required for the shift from locally excitable to noisy oscillatory dynamics in embryos depleted of formin but not anillin

Both formin and anillin depletion induce a transition to noisy oscillatory dynamics but with qualitatively distinct spatiotemporal patterns of RhoA excitation (Figures 1C and 4, E–G). Since local reduction in F-actin levels correlates with RhoA excitation in both cases (Figure 5, C and D), we reasoned that these differences in spatiotemporal RhoA excitation patterns could reflect differences in the mechanisms that drive local reduction in F-actin levels. Consistent with this possibility, we observed different patterns of actomyosin contractility in formin- and anillin-depleted embryos (Figure 7; Supplemental Movie S8). In *cyk-1(RNAi)* embryos, cycles of local actomyosin accumulation and disappearance are correlated with local contraction and dilation, respectively (Figure 7B; blue arrows indicate accumulation/contraction; orange asterisks indicate disappearance/dilation). Accumulation preceded contraction, while disappearance preceded cortical tearing and dilation, which was followed by another round of accumulation. These cycles were synchronized across large regions of the embryo (best seen in Supplemental Movie S7), matching the rapid recurrent spread of RhoA activity (Figure 4E). We observed very similar dynamics in profilin-depleted embryos (Supplemental Figure S6; Supplemental Movie S9). Recurrent cycles of local tearing followed by GFP::ROK accumulation and contraction were particularly apparent in embryos weakly depleted of profilin (Supplemental Figure S6; Supplemental Movie S9, left). In more strongly depleted embryos, the dynamics became increasingly chaotic (Supplemental Figure S6; Supplemental Movie S9, middle and right); however, the correlation between local tearing and subsequent accumulation and contraction of GFP::ROK persisted. By contrast, in *ani-1(RNAi)* embryos, F-actin and myosin II undergo cycles of accumulation and rapid disappearance with very little cortical movement (Figure 7).

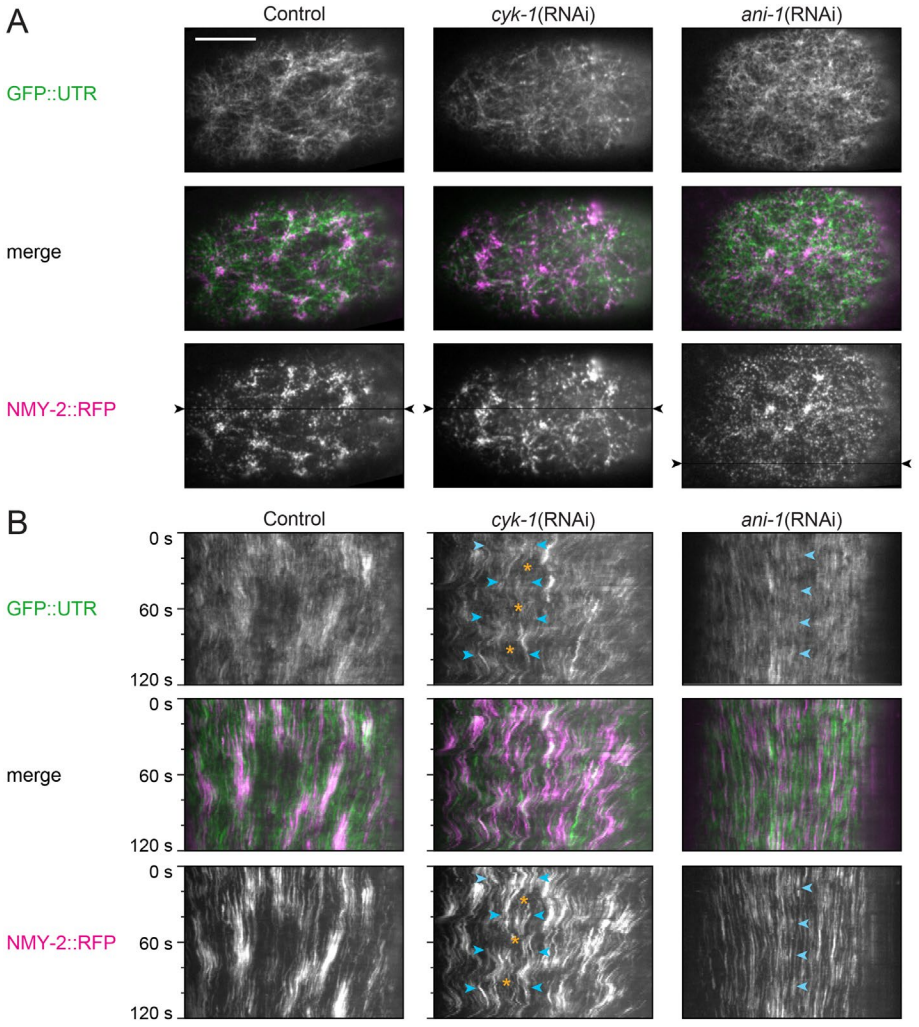

FIGURE 7: Distinct patterns of local contractility underlie the transition to noisy oscillatory dynamics in formin- and anillin-depleted embryos. (A) Single frames from the TIRF Supplemental Movies shown in Supplemental Movie S8 of embryos with the indicated perturbations expressing GFP::UTR and NMY-2::mKate2. Fluorescence intensities are scaled differently across perturbations to highlight actomyosin structures. (B) Kymographs from the same Supplemental Movies shown in A. Black arrowheads indicate the vertical position where each kymograph was generated. Paired cyan arrowheads overlaying the kymographs for *cyk-1(RNAi)* indicate a sequence of local contractions, each accompanied by accumulation of NMY-2::mKate2 and preceded by local cortical tearing/dilation events (orange asterisks). Cyan arrowheads overlaying the kymographs for *ani-1(RNAi)* indicate the recurrent accumulation of GFP::UTR and NMY-2::mKate2 without local contraction or dilation. Scale bar is 10 μm.

These observations suggest that actomyosin contractility could play different roles in producing the different spatiotemporal patterns of RhoA excitation in *cyk-1(RNAi)* and *ani-1(RNAi)* embryos. To test this possibility, we compared the effects of depleting formin and anillin in control [*spd-5(RNAi)*] embryos and in temperature-sensitive myosin mutant (*nmy-2(ts)* (Liu *et al.*, 2010) embryos produced at the restrictive temperature (25°C). Specifically, we compared the recurrence (excitation frequency and wait time distributions; Figure 8, A–F) and spatial pattern (cumulative area and duration of the largest linked excitation regions; Figure 8, G and H) of RhoA excitation. In *nmy-2(ts)* embryos observed at 25°C, the recurrence and spatial pattern of RhoA excitation were similar to those observed in controls (Figure 8, A, D, G, and H). Inhibiting myosin contractility in formin-depleted embryos [*cyk-1(RNAi); nmy-2(ts); 25°C*] produced a sharp decrease in the recurrence of RhoA excitation (Figure 8, B and E) and in the cumulative area and duration of linked excitation regions (Figure 8, G and H), indicating a loss of the spatial synchrony of RhoA excitation observed in *cyk-1(RNAi)* alone. The resulting dynamics were similar to those observed in *nmy-2(ts)* alone. In contrast, inhibiting myosin contractility in anillin-depleted embryos [*ani-1(RNAi); nmy-2(ts)*] produced dynamics similar to those observed in *ani-1(RNAi)* alone (Figure 8, C, F–H), except for a small increase in excitation frequency. Thus the shift toward spatially synchronized noisy oscillatory dynamics produced by depleting formin requires myosin II activity, while the shift toward noisy oscillations and the spatiotemporal patterns of spreading excitation produced by depleting anillin do not.

DISCUSSION

Pulsatile RhoA activity underlies the control of many different cell and tissue behaviors. Here we asked whether variations in spatial and temporal patterns of pulsatile RhoA activity observed in different contexts could be recapitulated in the *C. elegans* zygote by modulating actin network assembly dynamics, architecture, and contractility. We identified perturbations that induce variations along two axes: from locally excitable to noisy oscillatory temporal dynamics and from focal (standing) pulses to traveling waves. In particular, we found that reducing actin assembly rates by depleting formin/CYK-1 or profilin/PFN-1 induces a transition to locally oscillatory dynamics that are synchronized across larger cortical regions, while depleting anillin/ANI-1 induces spatiotemporal activity patterns that are reminiscent of, albeit more irregular than, the oscillatory propagating waves observed in other cells. Our analysis suggests that these pattern variants can be understood as a consequence of changes in local F-actin dynamics, leading to different dynamics of RhoA inhibition.

Reduced levels and faster depletion of F-actin induce a shift from excitable to noisy oscillatory dynamics

In simple activator/inhibitor systems, transitions from excitable to oscillatory dynamics can be induced by decreasing the overall level of inhibition or by enhancing the release of inhibition following a pulse. Consistent with these possibilities, we find that i) the overall density of F-actin is reduced in formin- and anillin-depleted embryos relative to controls and ii) on average, local depletion of F-actin precedes pulse initiation in formin- and anillin-depleted embryos but not in controls. Thus we propose that in control embryos, higher overall levels of F-actin set a higher threshold for pulse initiation, making it hard to trigger pulses through local fluctuations in RhoA activity or F-actin levels. In formin- and anillin-depleted embryos, lower overall levels of F-actin and faster and stronger

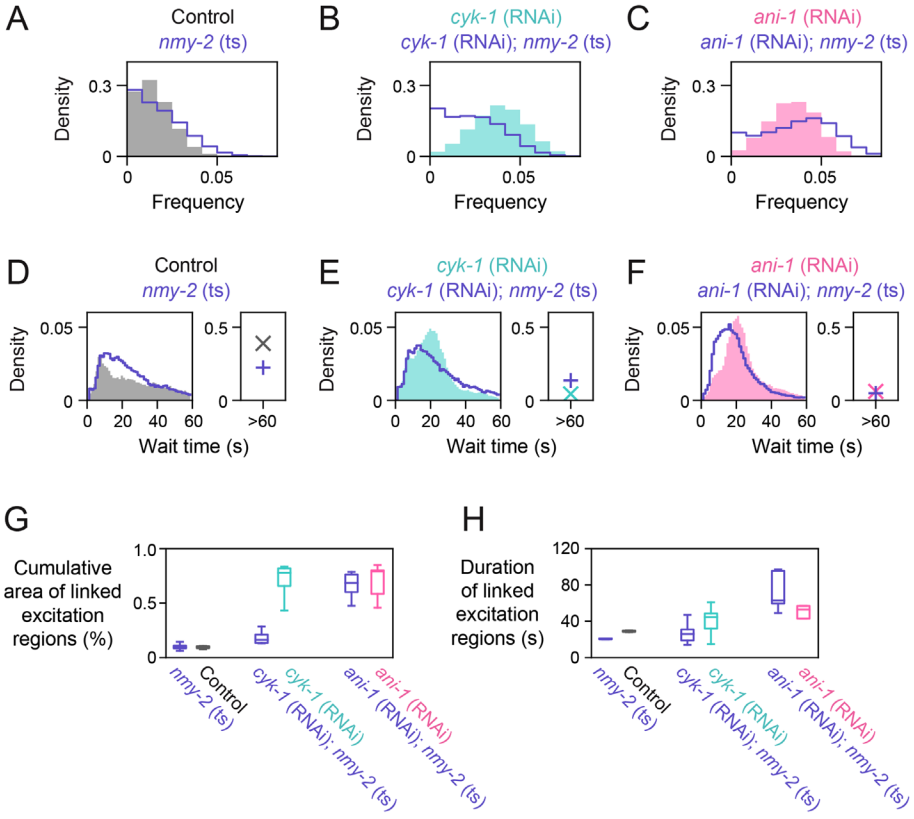

FIGURE 8: Contractility is required for the shift from locally excitable to noisy oscillatory dynamics in embryos depleted of formin but not anillin. (A–C) Distributions of excitation frequencies for all pixels in embryos with the indicated perturbations. Filled histograms show the data from Figure 3C. Overlaid blue histograms show the data from *nmy-2(ts)* embryos alone (A, for comparison with *spd-5(RNAi)* controls) or in combination with formin (B) or anillin (C) depletion. (D–F) Distributions of wait times between new excitations for all new excitation events in embryos with the indicated perturbations. Filled histograms show the data from Figure 3D. Overlaid blue histograms show the data from *nmy-2(ts)* embryos alone (D, for comparison with spd-5(RNAi) controls) or in combination with formin (E) or anillin (F) depletion. (G) Box plots showing the distribution of cumulative areas of the largest linked groups in embryos with the indicated perturbations. (H) Box plots showing the duration of the largest linked groups in embryos with the indicated perturbations. The number of embryos used for analysis in A–H are control/*spd-5(RNAi)* (6), *spd-5(RNAi);cyk-1(RNAi)* ($n = 8$). *spd-5(RNAi);ani-1(RNAi)* ($n = 5$), *nmy-2(ts)* ($n = 7$), *nmy-2(ts); cyk-1(RNAi)* ($n = 5$), *nmy-2(ts); ani-1(RNAi)* ($n = 7$).

depletion of F-actin after a pulse drive a shift to locally oscillatory pulse dynamics.

Distinct mechanisms for local F-actin depletion distinguish different spatiotemporal pulse dynamics induced by formin and anillin depletion

In embryos depleted of formin or profilin, local dilation of the cortex precedes the initiation and spread of RhoA activity; in cyk-1(RNAi) [and likely pfn-1(RNAi)] embryos, these dilations do not occur in the absence of contractility. We propose that the noisy oscillations induced by formin or weak profilin depletion are driven by coupling excitable RhoA dynamics with a local cortical tearing instability. As RhoA, F-actin, and myosin II disappear locally following a pulse, reduced contractility (and connectivity) relative to neighboring regions induces local dilation, cortical tearing, and further depletion of F-actin, and this in turn leads to rapid RhoA activation and new pulse initiation. Accumulation of F-actin at the edges of dilated regions may ultimately limit this spread to produce larger but still spatially restricted pulses of RhoA activity. Whether RhoA activation is purely a response to local reduction in F-actin levels or involves a more complicated mechanical response to network tearing, as observed in other contexts (Smith *et al.*, 2010; Sun *et al.*, 2020; Winkelman *et al.*, 2020), remains to be determined.

The instabilities that we observe in formin- and profilin-depleted embryos are reminiscent of cortical tearing instabilities that underlie bleb formation and cell shape oscillations in other cells (Paluch *et al.*, 2005; Charras and Paluch, 2008). Interestingly, spontaneous local tearing occurs with low frequency in both wild-type (Mayer *et al.*, 2010) and SPD–5-depleted zygotes (Figure 6B; Supplemental Movies S7 and S8), suggesting that *C. elegans* zygotes are poised close to such a tearing instability. Thus we propose that reducing rates of filament assembly by formin or profilin depletion increases the tendency for local depletion of F-actin after a pulse to trigger a local contractility instability and re-excitation of RhoA, leading to oscillatory dynamics.

A related behavior occurs in epithelial cells of gastrula stage frog embryos, where local breakage of tight junctions along contractile cell–cell contacts leads to the production of local RhoA pulses (called "flares" in this system), which in turn promote local assembly of actomyosin to repair the break (Reyes *et al.*, 2014; Stephenson *et al.*, 2019). In this system, local depletion of tight junction components, but not F-actin, precedes spontaneously occurring RhoA flares. However, reducing F-actin assembly rates by treating embryos with Latrunculin can induce local tearing instabilities that result in local depletion of both F-actin and tight junction components and recurrent activation of RhoA flares (Reyes *et al.*, 2014; Stephenson *et al.*, 2019), similar to what we describe here in *C. elegans* embryos depleted of formin or profilin. Together these observations highlight a general route to oscillatory RhoA dynamics in contractile systems by enhancing the tendency toward tearing instabilities in the presence of a Rho-based repair mechanism.

By contrast, in anillin-depleted embryos, F-actin and myosin II disappear rapidly after each pulse in the absence of significant cortical contractions or dilations. Our analysis suggests that the rapid depletion of F-actin promotes local oscillations in anillin-depleted embryos, but in the absence of cortical tearing instabilities, these oscillations are not synchronized across larger cortical regions. Instead, asynchronous oscillations create local zones of F-actin depletion in neighboring regions, and these appear to serve as channels through which activation can propagate (Supplemental Movie S6), allowing continuous exploration of the cortex by locally propagating wavefronts.

What drives the rapid disappearance of F-actin in anillin-depleted embryos? Previous studies have shown that the rate of F-actin disassembly increases before the initiation of RhoA pulses in early *C. elegans* embryos (Michaux *et al.*, 2018). Anillin accumulates

locally during individual pulses (Tse *et al.*, 2011; Michaux *et al.*, 2018), and studies in *C. elegans* larvae and in vitro suggest that anillin can stabilize F-actin by antagonizing the severing activity of cofilin/UNC-60A (Tian *et al.*, 2015). If anillin plays a similar role in stabilizing F-actin during individual pulses, then increased disassembly on its removal could explain the more rapid depletion that we observe. Anillin has also been shown to promote formin-dependent actin assembly in some contexts (Watanabe *et al.*, 2010), and thus local reduction in F-actin assembly may also contribute to the more rapid depletion of F-actin in anillin-depleted embryos. Local measurements of actin filament assembly/disassembly (Robin *et al.*, 2014) will allow us to distinguish these and other possibilities in future studies.

A comparison with previous observations of RhoA dynamics in polarizing zygotes

Nishikawa *et al* (2017) described pulsatile dynamics of RhoA activation, myosin II accumulation, and cortical flow in polarizing *C. elegans* zygotes. They hypothesized that these dynamics arise through coupling between an autonomous (actomyosin-independent) RhoA oscillator and a form of contractile instability in which RhoA promotes myosin-dependent contractile flows which in turn advect and concentrate RhoA. In Nishikawa *et al.* (2017), oscillatory dynamics were inferred from cross-correlation analysis at the posterior cortex of polarizing zygotes that are undergoing long-range pulsatile flows (Munro *et al.*, 2004; Mayer *et al.*, 2010; Nishikawa *et al.*, 2017; Naganathan *et al.*, 2014). In these embryos, posterior RhoA activity is modulated by signals associated with the sperm-derived centrosomes in addition to negative feedback from F-actin/RhoGAPs (Cowan and Hyman, 2004; Motegi and Sugimoto, 2006; Kapoor and Kotak, 2019; Zhao *et al.*, 2019; reviewed in Bolado-Carrancio *et al.*, 2020).

Here we used *spd-5(RNAi)* to block the centrosome-dependent inhibition of RhoA and the confounding effects of long-range flows, and we used an alternative approach to analyze pulsatile dynamics in which we track the local recurrence and propagation of excitation events. Our current analysis and previous work (Michaux *et al.*, 2018) suggest that in these conditions, pulsatile RhoA dynamics are intrinsically excitable, not oscillatory, although we cannot exclude the possible existence of low amplitude oscillations that lie below our threshold for detecting the rapid rise in RhoA activity during pulse initiation. Moreover, during individual pulses in SPD–5-depleted zygotes, or in AB cells that do not polarize, the rapid rising phase of RhoA activation precedes the onset of local contraction (Michaux *et al.*, 2018), arguing against a contractile instability in which local contraction concentrates RhoA. Instead, our data reveal an alternative mechanism by which coupling a cortical tearing instability to excitable RhoA dynamics through local F-actin depletion can induce oscillatory pulse dynamics. It will be interesting to see how this mechanism contributes to shaping pulsatile flow dynamics during polarization.

What controls the initiation and spread of RhoA pulses in control embryos?

Our data suggest that the higher overall levels of F-actin in control embryos increase the threshold for initiation of RhoA pulses and reduce the frequency with which they occur. Pulses still tend to form and spread within "depletion regions" containing lower levels of F-actin, consistent with an inhibitory role for F-actin. However, the relationship between local F-actin depletion and RhoA excitations is more complex. In some cases, as discussed above, local depletion of F-actin by cortical tearing appears to trigger RhoA pulses. But in many other cases, RhoA pulses initiate at the edges of depletion regions near existing RhoA foci in regions where F-actin levels are persistently high. We hypothesize that these foci serve as local sources of active RhoA that can diffuse into and trigger pulses in adjacent regions containing lower levels of F-actin. However, it remains unclear how RhoA activity can persist in and even spread through regions with high levels of F-actin. One possibility that we will explore in future studies is that one or more additional positive feedback loops, perhaps involving anillin (Maddox *et al.*, 2007; Budnar *et al.*, 2019), could locally counter the inhibitory effects of F-actin.

It also remains unclear what restricts the spread of active RhoA to produce focal pulses in control embryos. Simple activator/inhibitor models predict that if active RhoA can freely diffuse while the inhibitory GAPs RGA-3/4 are immobilized through binding to F-actin, then RhoA pulses should tend to propagate as waves. In principle, focal pulses could be achieved by reducing the spread of activation and/or increasing the spread of inhibition. Higher overall levels of F-actin could limit the speed at which RhoA excitation spreads in control embryos. Alternatively, local binding of active RhoA to its effectors (e.g., anillin/ANi-1 and formin/CYK-1) could reduce its effective mobility. However, these effects are likely to be small, because we observe only small differences in distribution of speeds at which RhoA activation spreads locally in control versus formin- and anillin-depleted embryos. It is also possible that local differences in F-actin architecture could shape its ability to inhibit the spread of RhoA (Bement *et al.*, 2015; Michaud *et al.*, 2021). For example, the F-actin bundles that bound depletion regions could in principle provide more effective inhibition than a more diffuse network. However, pulses remain focal in nmy-2(ts) embryos that lack robust F-actin bundles. Finally, recent work suggests that during pulse initiation, active RhoA recruits cytoplasmic formin/CYK-1 in pulsing regions that subsequently elongate filaments at ~1.5 μm/s (Costache *et al.*, 2021; Li and Munro, 2021). Thus in principle, rapid filament elongation could project a zone of F-actin assembly beyond the front of active RhoA and limit its spread. It will be interesting to test these and other possibilities in future studies.

Concluding remarks

In conclusion, our work highlights the importance of actomyosin dynamics in shaping spatiotemporal patterns of pulsatile RhoA activity. It suggests that some of the different patterns of activity observed in other cellular or developmental contexts could arise from differences in the underlying actomyosin dynamics. It also highlights the inadequacy of very simple models for explaining the rich diversity and heterogeneity of pulsatile dynamics observed in living cells or more recently in. While deeper understanding may require the identification and characterization of additional feedback loops, it will likely also require the use of new experimental approaches, such as the use of cell free cytoplasmic extracts (Landino *et al.*, 2021) and/or more detailed models that consider the complex and heterogeneous dynamics of the actomyosin cytoskeleton which forms the physical scaffold on which these dynamics unfold.

MATERIALS AND METHODS

Request a protocol through *Bio-protocol*.

C. elegans culture and strains

We cultured *C. elegans* strains at 22°C under standard conditions (Brenner, 1974). Table 1 lists the mutations and transgenes used in this study. Unless otherwise specified, strains were provided by the Caenorhabditis Genetics Center, which is funded by the National Institutes of Health National Center for Research Resources.

Strain label	Strain name	Genotype	Source
GFP::LET-502; Lifeact::mCherry	EM367	mc74(GFP::let-502)I; zbIs2[pie-1::Lifeact::mCherry, unc-119(+)]	This study
GFP::LET-502; *nmy-2(ts)*	EM369	mc74(GFP::let-502)I; NMY-2(ne1490) I	This study
GFP::UTR; NMY-2::mRFP	EM101	zuIs151[nmy-2::NMY-2::mRFP, unc-119(+)]; mgSi3[cb-UNC-119 (+) GFP::UtrophinABD]II	Michaux *et al.*, 2018

TABLE 1

RNAi

We performed RNAi using the feeding method as previously described (Timmons *et al.*, 2001). We obtained bacteria targeting spd-5, cyk-1, and pfn-1 from the Kamath feeding library (Kamath *et al.*, 2003). The bacteria targeting ani-1 is from the Glotzer lab at the University of Chicago. The RNAi sequence spans residues 40–170 aa and is cloned into the KpnI site of L4440. Briefly, we grew bacteria to log phase in LB with 50 µg/ml ampicillin and then seeded ~300 µl of these bacteria onto NGM plates supplemented with 50 µg/ml ampicillin and 1 mM IPTG. For double RNAi treatments, we grew the bacteria for both treatments separately to log phase, mixed equal volumes of the individual bacteria cultures and then seeded ~300 µl of culture onto NGM plates supplemented with 50 µg/ml ampicillin and 1 mM IPTG. We incubated the seeded plates at room temperature (21–23°C) for 2 d and then stored them at 4°C for up to 1 wk before use. We transferred L4 larvae to feeding plates and then cultured them at room temperature (21–23°C) for GFP::ROK; Lifeact::mCherry and GFP::UTR; NMY-2::mRFP and at 16°C for GFP::ROK; *nmy-2(ts)*. Please note that the culture time for each feeding strain is listed in Table 2.

Feeding RNAi targets	Feeding times
spd-5 (RNAi)	16–22 h
spd-5 (RNAi); cyk-1 (RNAi)	14–18 h
spd-5 (RNAi); ani-1 (RNAi)	24–28 h
spd-5 (RNAi); pfn-1 (RNAi)	8–22 h
spd-5 (RNAi); mel-11 (RNAi)	16–22 h
spd-5 (RNAi); unc-60 (RNAi)	16–22 h

TABLE 2

Microscopy

We performed imaging on a Nikon Ti-E inverted microscope equipped with a Yokogawa CSU-X1 spinning disk scan head, a motorized TIRF illuminator, and a Ti-ND6-PFS Perfect Focus Unit. A laser merge module (Spectral Applied Research) controlled tunable delivery of 481-nm and 561-nm laser excitation from 50 mW solid-state lasers (Coherent Technology) to either the confocal scanhead or the TIRF illuminator with fast (ms) control of laser power and switching between lasers. All image acquisition was controlled by Metamorph software. We collected images using a Nikon CFI Apo 1.45 NA oil immersion objective combined with 1.5× intermediate magnification onto an Andor iXon3 897 EMCCD camera.

Imaging conditions

We mounted embryos as described previously (Sailer *et al.*, 2015) in 3–5 µl of standard egg salts (118 mM NaCl, 48 mM KCl, 3 mM CaCl2, 3 mM MgCl2, 5 mM HEPES, pH 7.2) on 3% agarose pads (3% agarose in standard egg salts) under #1.5 coverslips. For all experiments, we imaged embryos in early establishment phase (mitotic interphase), during which there is no qualitative change in pulsatile RhoA dynamics in control [*spd-5(RNAi)*] embryos. To quantify patterns of RhoA excitation and correlations with F-actin levels under different RNAi perturbations, we used a strain coexpressing GFP::ROK (Bell *et al.*, 2020) and Lifeact::mCherry (Pohl *et al.*, 2012). To quantify patterns of RhoA excitation in a myosin mutant background in response to different RNAi perturbations, we used a temperature-sensitive myosin mutant strain [(*myo(ts)*; Liu *et al.*, 2010] expressing GFP::ROK. For both experiments, we used spinning disk confocal imaging and alternated between 488 nm (30% laser power, 300 ms exposure time) and 561 nm (50% laser power, 300 ms exposure time) excitation. To visualize actomyosin network dynamics in response to different RNAi perturbations, we imaged worms expressing mKate::NMY-2 and GFP::UTR with near-TIRF illumination as described previously (Li and Munro, 2021), alternating between 488 nm (20% laser power, 200 ms exposure time) and 561 nm (30% laser power, 200 ms exposure time) excitation. To visualize GFP::ROK and F-actin in control [*spd-5(RNAi)*] embryos, we used near-TIRF illumination, alternating between 488 nm (30% laser power,300 ms exposure time) and 561 nm (50% laser power, 300 ms exposure time) excitation. We performed all imaging experiments at room temperature (21–23°C), except for temperature-sensitive myosin mutants (*myo(ts)*, which we imaged at 25°C.

Kymograph analysis

To produce the kymographs shown in Figures 1C, 2E, 5B, and 7B and Supplemental Figures S1, S2, S5A, and S6B, we rotated images so that the anterior–posterior axis of the embryo coincided with the horizontal (x) image axis. We selected rectangular regions aligned with the x image axis whose width (in x) coincided with the embryonic ROI and whose height (in y) was 10 pixels. From the original image stack, we extracted an xyt substack corresponding to this rectangular region; we resliced this stack with respect to the xt plane, and then we used a maximum-intensity projection to collapse the individual slices in y to obtain a kymograph in x versus t.

Image analysis

We performed all image processing using custom functions written in Python. The code is available at https://github.com/baixue0/excitability. We developed custom image segmentation algorithms to identify regions of RhoA excitation in noisy microscopy images by thresholding the temporal derivative of smoothed GFP::ROK intensities. This approach transforms ROK levels to binary masks, allowing us to quantify the temporal recurrence and spatial spread of RhoA excitation at pixel resolution.

Segmenting regions of RhoA excitation

We performed all analyses described below on data collected within a standard observation window lasting 120 s. To correct for photobleaching, we measured M1(n), the mean intensity of ROK::GFP for all pixels in the embryo at frame n over the 120 s observation window ($n = 1, 2, \ldots, 100$ frames). We then calculated its temporal trend M2(n) by applying the Scipy filter savgol_filter (window_length = 6 s,

polyorder = 1) to M1(n). To calculate the correction factor C(n), we subtracted M2(n) from its mean value. We then added C(n) to the raw intensity value for each pixel at frame n.

To determine local regions of RhoA excitation within individual frames, we first smoothed each frame of the image stack in space and time. We smoothed in space using sequential application of the Scipy functions medianBlur (5 pixels diameter) and GaussianBlur (19 pixels diameter). We smoothed in time using sequential application of a 5-frame centered moving average, followed by a 2-frame grouped average). We then computed a pixelwise temporal difference signal using a 5-frame (6s) window centered on the current frame. We set the derivative time window to be half the duration of the rapid rising phase so that short-lived intensity fluctuations from other sources were suppressed. Then we scaled the temporal difference values at each pixel by the standard deviation of the temporal difference, taken over all pixels in all frames, to obtain the normalized temporal difference. Finally, we thresholded the normalized temporal difference at each pixel to obtain a binary mask with 1 representing pixels above threshold and 0 representing below threshold.

To determine appropriate threshold values, for each phenotype we measured the average normalized temporal difference signal within manually labeled pulsing regions (~25 disks with 1 μm diameter per embryo) over the duration of a pulse. We used 40% of the average peak signal for all conditions, which captured distinct pulses with different amplitudes while excluding noisy fluctuations.

Using these binary masks, we defined *excitation pixels* as pixels that are above the threshold in the current frame and *new excitation pixels* as pixels that are above threshold in the current frame, but below the threshold in the previous frame. Similarly, in a given frame, we defined *excitation regions* as contiguous groups of excitation pixels and *new excitation regions* as contiguous groups of new excitation pixels.

Measuring the distribution of frequency and wait times between successive new excitations

We computed the distribution of frequencies over all pixels by counting the number of excitation events recorded at each pixel and dividing by the duration of the observation time window. For each new excitation event at a given pixel, we monitored the pixel's excitation state over the following 60 s. If we detected a new excitation event within 60 s, we computed the wait time as the difference between the first and the second excitation times. We thus report the fraction of pixels for which the wait time >60 s and the distribution of wait times over all pairs of excitation events with wait times <60 s.

Linking excitation regions across frames

We considered two excitation regions to be linked across consecutive frames if their area of overlap was greater than 8 pixels and greater than 10% of the total area of both regions. Note that this definition allows merging and splitting of excitation regions. We compute linked excitation regions by extending pairwise linkage recursively, backward and forward in time using the connected_components function from the Python package networkx. To compute the duration of linked excitation regions, we determined the first frame (f_0) and the last frame (f_l) in which an individual excitation region belonging to the linked group appeared. Then we computed duration = $1.2*(f_l–f_0)$. To plot the cumulative area of linked excitation regions versus time, for each frame f in the image sequence we computed the total number of unique pixels belonging to excitation regions appearing in frames preceding f. To determine the total areas, we computed the total number of unique pixels belonging to all excitation regions.

Measuring the speed of advance of local excitation fronts

In each frame, we identified the boundaries of excitation regions whose area was larger than 0.04 μm^2. We identified a set of points spaced at ~0.5-μm intervals along the boundary. We considered that a boundary point belongs to an excitation front if it lies within a new excitation region. For every boundary point along an excitation front, we constructed a local displacement vector extending from that point, outward normal to the boundary, and intersecting the nearest excitation boundary in the next frame. We then took the instantaneous speed of advance to be the length of this displacement vector divided by time between frames (1.2 s). We divided boundary points into "fast" and "slow" groups based on instantaneous velocity using 0.25 μm/s as a threshold.

Sampling pixels ahead of advancing excitation fronts

At each time point, we selected all boundary points belonging to excitation fronts. For each point, we defined a rectangular region extending 0.5 μm from the boundary point in the outward normal direction (i.e., ahead of the advancing front) and extending 0.6 μm in the perpendicular direction centered on the boundary point. Then we sampled F-actin intensity values or time derivatives on all pixels within the rectangular region at different times relative to the current time point; that is, relative to when the advancing front begins to enter the rectangular region—which we refer to as "time of entry." We constructed plots of average F-actin intensity or time derivatives relative to time of entry for "fast" and "slow" advancing fronts by averaging these measurements over all "fast" or "slow" boundary points.

Measuring the tACF of GFP::ROK intensities

For each pixel in the embryo, we extracted a time series of smoothed ROK intensities measured at 1.2-s intervals over 120 s. Then we computed the standard time autocorrelation function (tACF) using the Python package statsmodels.tsa.stattools.acf. The tACF shown in Supplemental Figure S3 is the average over all pixels in embryos of a given phenotype.

Simulating the temporal dynamics of the FHN model with stochastic forcing

We considered a nonspatial stochastic version of the FHN model (equations shown in Supplemental Figure S4A), where ξ_t defines a random sequence of perturbations, each described by a rectangle function R(h,d) with amplitude h = 0.1 and duration d = 3 s. For each simulation, we selected seven initiation times randomly from a uniform probability distribution over the simulation time window (0–240 s), yielding an average perturbation frequency of 0.03/s. We fixed values for parameters (I = 0.5, b = 0.6, τ = 10) and then varied the value of α to tune the deterministic dynamics of the system from excitable to oscillatory. For each value of α, we repeated the simulation 16,384 times. For each simulation, we thresholded the temporal derivative of u to identify individual excitation events. Then we computed frequency and wait time distributions using the same method described above for RhoA excitations.

ACKNOWLEDGMENTS

We thank Katrina Longhini and Michel Labouesse for worm strains and RNAi feeding strains; Mike Rust, Aaron Dinner, Edwin Ferguson, and members of the Munro laboratory for valuable discussions; and

Katrina Longini for technical assistance. This work was supported by the National Institute of General Medical Sciences R01GM098441 to Ed Munro.

REFERENCES

Allard J, Mogilner A (2013). Traveling waves in actin dynamics and cell motility. Curr Opin Cell Biol 25, 107–115.

Arai Y, Shibata T, Matsuoka S, Sato MJ, Yanagida T, Ueda M (2010). Self-organization of the phosphatidylinositol lipids signaling system for random cell migration. Proc Natl Acad Sci USA 107, 12399–12404.

Azevedo D, Antunes M, Prag S, Ma X, Hacker U, Brodland GW, Hutson MS, Solon J, Jacinto A (2011). DRhoGEF2 regulates cellular tension and cell pulsations in the Amnioserosa during Drosophila dorsal closure. Plos One 6, e23964.

Baird MA, Billington N, Wang A, Adelstein RS, Sellers JR, Fischer RS, Waterman CM (2017). Local pulsatile contractions are an intrinsic property of the myosin 2A motor in the cortical cytoskeleton of adherent cells. Mol Biol Cell 28, 240–251.

Bell KR, Werner ME, Doshi A, Cortes DB, Sattler A, Vuong-Brender T, Labouesse M, Maddox AS (2020). Novel cytokinetic ring components drive negative feedback in cortical contractility. Mol Biol Cell 31, 1623–1636.

Bement WM, Leda M, Moe AM, Kita AM, Larson ME, Golding AE, Pfeuti C, Su KC, Miller AL, Goryachev AB, *et al.* (2015). Activator-inhibitor coupling between Rho signalling and actin assembly makes the cell cortex an excitable medium. Nat Cell Biol 17, 1471–1483.

Bhattacharya S, Banerjee T, Miao Y, Zhan H, Devreotes PN, Iglesias PA (2020). Traveling and standing waves mediate pattern formation in cellular protrusions. Sci Adv 6, eaay7682.

Blanchard GB, Étienne J, Gorfinkiel N (2018). From pulsatile apicomedial contractility to effective epithelial mechanics. Curr Opin Genet Dev 51, 78–87.

Bolado-Carrancio A, Rukhlenko OS, Nikonova E, Tsyganov MA, Wheeler A, Garcia-Munoz A, Kolch W, von Kriegsheim A, Kholodenko BN (2020). Periodic propagating waves coordinate RhoGTPase network dynamics at the leading and trailing edges during cell migration. ELife 9, e58165.

Brabant G, Prank K, Schofl C (1992). Pulsatile patterns in hormone secretion. Trends Endocrinol Metab 3, 183–190.

Brenner S (1974). The genetics of Caenorhabditis elegans. Genetics 77, 71–94.

Budnar S, Husain KB, Gomez GA, Naghibosadat M, Varma A, Verma S, Hamilton NA, Morris RG, Yap AS (2019). Anillin promotes cell contractility by cyclic resetting of RhoA residence kinetics. Dev Cell 49, 894–906.e12.

Charras G, Paluch E (2008). Blebs lead the way: how to migrate without lamellipodia. Nat Rev Mol Cell Biol 9, 730–736.

Clay JR (2005). Axonal excitability revisited. Prog Biophys Mol Biol 88, 59–90.

Costache V, Garcia SP, Plancke CN, Li J, Begnaud S, Suman SK, Reymann A-C, Kim T, Robin FB (2021). Rapid assembly of a polar network architecture drives efficient actomyosin contractility. bioRxiv, 2020.12.08.406298.

Cowan CR, Hyman AA (2004). Centrosomes direct cell polarity independently of microtubule assembly in *C. elegans* embryos. Nature 431, 92–96.

Dickinson DJ, Schwager F, Pintard L, Gotta M, Goldstein B (2017). A single-cell biochemistry approach reveals PAR complex dynamics during cell polarization. Dev Cell 42, 416–434.e11.

DiFrancesco D (1993). Pacemaker mechanisms in cardiac tissue. Annu Rev Physiol 55, 455–472.

Ding WY, Ong HT, Hara Y, Wongsantichon J, Toyama Y, Robinson RC, Nédélec F, Zaidel-Bar R (2017). Plastin increases cortical connectivity to facilitate robust polarization and timely cytokinesis. J Cell Biol 216, 1371–1386.

Dockery JD, Keener JP (1989). Diffusive effects on dispersion in excitable media. SIAM J Appl Math 49, 539–566.

Ermentrout GB, Hastings SP, Troy WC (1984). Large amplitude stationary waves in an excitable lateral-inhibitory medium. SIAM J Appl Math 44, 1133–1149.

Gorfinkiel N, Blanchard GB, Adams RJ, Martinez Arias A (2009). Mechanical control of global cell behaviour during dorsal closure in Drosophila. Development 136, 1889–1898.

Graessl M, Koch J, Calderon A, Kamps D, Banerjee S, Mazel T, Schulze N, Jungkurth JK, Patwardhan R, Solouk D, *et al.* (2017). An excitable Rho GTPase signaling network generates dynamic subcellular contraction patterns. J Cell Biol 216, 4271–4285.

Hamill DR, Severson AF, Carter JC, Bowerman B (2002). Centrosome maturation and mitotic spindle assembly in *C. elegans* require SPD-5, a protein with multiple coiled-coil domains. Dev Cell 3, 673–684.

Hecht I, Kessler DA, Levine H (2010). Transient localized patterns in noise-driven reaction-diffusion systems. Phys Rev Lett 104, 158301.

Huang C-H, Tang M, Shi C, Iglesias PA, Devreotes PN (2013). An excitable signal integrator couples to an idling cytoskeletal oscillator to drive cell migration. Nat Cell Biol 15, 1307–1316.

Kamath RS, Fraser AG, Dong Y, Poulin G, Durbin R, Gotta M, Kanapin A, Le Bot N, Moreno S, Sohrmann M, *et al.* (2003). Systematic functional analysis of the Caenorhabditis elegans genome using RNAi. Nature 421, 231–237.

Kapoor S, Kotak S (2019). Centrosome Aurora A regulates RhoGEF ECT-2 localisation and ensures a single PAR-2 polarity axis in *C. elegans* embryos. Development 146, dev174565.

Klaasen GA, Troy WC (1984). Stationary wave solutions of a system of reaction-diffusion equations derived from the Fitzhugh–Nagumo equations. SIAM J Appl Math 44, 96–110.

Koga S, Kuramoto Y (1980). Localized patterns in reaction-diffusion systems. Prog Theor Phys 63, 106–121.

Landino J, Leda M, Michaud A, Swider ZT, Prom M, Field CM, Bement WM, Vecchiarelli AG, Goryachev AB, Miller AL (2021). Rho and F-actin self-organize within an artificial cell cortex. Curr Biol 31, 5613–5621.

Levine JH, Lin Y, Elowitz MB (2013). Functional roles of pulsing in genetic circuits. Science 342, 1193–1200.

Li Y, Munro E (2021). Filament-guided filament assembly provides structural memory of filament alignment during cytokinesis. Dev Cell 56, 2486–2500.

Liu J, Maduzia LL, Shirayama M, Mello CC (2010). NMY-2 maintains cellular asymmetry and cell boundaries, and promotes a SRC-dependent asymmetric cell division. Dev Biol 339, 366–373.

Maddox AS, Habermann B, Desai A, Oegema K (2005). Distinct roles for two *C. elegans* anillins in the gonad and early embryo. Development 132, 2837–2848.

Maddox AS, Lewellyn L, Desai A, Oegema K (2007). Anillin and the septins promote asymmetric ingression of the cytokinetic furrow. Dev Cell 12, 827–835.

Maître J-L, Niwayama R, Turlier H, Nédélec F, Hiiragi T (2015). Pulsatile cell-autonomous contractility drives compaction in the mouse embryo. Nat Cell Biol 17, 849–855.

Mayer M, Depken M, Bois JS, Jülicher F, Grill SW (2010). Anisotropies in cortical tension reveal the physical basis of polarizing cortical flows. Nature 467, 617–621.

Meron E (1992). Pattern formation in excitable media. Phys Rep 218, 1–66.

Michaud A, Swider ZT, Landino J, Leda M, Miller AL, von Dassow G, Goryachev AB, Bement WM (2021). Cortical excitability and cell division. Curr Biol 31, R553–R559.

Michaux JB, Robin FB, McFadden WM, Munro EM (2018). Excitable RhoA dynamics drive pulsed contractions in the early *C. elegans* embryo. J Cell Biol 217, 4230–4252.

Motegi F, Sugimoto A (2006). Sequential functioning of the ECT-2 RhoGEF, RHO-1 and CDC-42 establishes cell polarity in Caenorhabditis elegans embryos. Nat Cell Biol 8, 978–985.

Munjal A, Philippe J-M, Munro E, Lecuit T (2015). A self-organized biomechanical network drives shape changes during tissue morphogenesis. Nature 524, 351–355.

Munro E, Nance J, Priess JR (2004). Cortical flows powered by asymmetrical contraction transport PAR proteins to establish and maintain anterior-posterior polarity in the early *C. elegans* embryo. Dev Cell 7, 413–424.

Murthy K, Wadsworth P (2008). Dual role for microtubules in regulating cortical contractility during cytokinesis. J Cell Sci 121, 2350–2359.

Naganathan SR, Fürthauer S, Rodriguez J, Fievet BT, Jülicher F, Ahringer J, Cannistraci CV, Grill SW (2018). Morphogenetic degeneracies in the actomyosin cortex. eLife 7, e37677.

Nagumo J, Arimoto S, Yoshizawa S (1962). An active pulse transmission line simulating nerve axon. Proc IRE 50, 2061–2070.

Neidt EM, Scott BJ, Kovar DR (2009). Formin differentially utilizes profilin isoforms to rapidly assemble actin filaments. J Biol Chem 284, 673–684.

Neidt EM, Skau CT, Kovar DR (2008). The cytokinesis formins from the nematode worm and fission yeast differentially mediate actin filament assembly. J Biol Chem 283, 23872–23883.

Nishikawa M, Naganathan SR, Jülicher F, Grill SW (2017). Controlling contractile instabilities in the actomyosin cortex. ELife 6, e19595.

Ono K, Parast M, Alberico C, Benian GM, Ono S (2003). Specific requirement for two ADF/cofilin isoforms in distinct actin-dependent processes in Caenorhabditis elegans. J Cell Sci 116, 2073–2085.

Pacquelet A, Uhart P, Tassan J-P, Michaux G (2015). PAR-4 and anillin regulate myosin to coordinate spindle and furrow position during asymmetric division. J Cell Biol 210, 1085–1099.
Paluch E, Piel M, Prost J, Bornens M, Sykes C (2005). Cortical actomyosin breakage triggers shape oscillations in cells and cell fragments. Biophys J 89, 724–733.
Piekny AJ, Glotzer M (2008). Anillin is a scaffold protein that links RhoA, actin, and myosin during cytokinesis. Curr Biol 18, 30–36.
Piekny AJ, Johnson J-LF, Cham GD, Mains PE (2003). The Caenorhabditis elegans nonmuscle myosin genes nmy-1 and nmy-2 function as redundant components of the let-502/Rho-binding kinase and mel-11/myosin phosphatase pathway during embryonic morphogenesis. Development 130, 5695–5704.
Pohl C, Tiongson M, Moore JL, Santella A, Bao Z (2012). Actomyosin-based Self-organization of cell internalization during *C. elegans* gastrulation. BMC Biol 10, 94.
Rauzi M, Lenne P-F, Lecuit T (2010). Planar polarized actomyosin contractile flows control epithelial junction remodelling. Nature 468, 1110–1114.
Reyes CC, Jin M, Breznau EB, Espino R, Delgado-Gonzalo R, Goryachev AB, Miller AL (2014). Anillin regulates cell-cell junction integrity by organizing junctional accumulation of Rho-GTP and actomyosin. Curr Biol CB 24, 1263–1270.
Ridley AJ (2015). Rho GTPase signalling in cell migration. Curr Opin Cell Biol 36, 103–112.
Robin FB, McFadden WM, Yao B, Munro EM (2014). Single-molecule analysis of cell surface dynamics in Caenorhabditis elegans embryos. Nat Methods 11, 677–682.
Rodriguez J, *et al*. (2017). aPKC Cycles between functionally distinct PAR protein assemblies to drive cell polarity. Dev Cell 42, 400–415.e9.
Roh-Johnson M, Shemer G, Higgins CD, McClellan JH, Werts AD, Tulu US, Gao L, Betzig E, Kiehart DP, Goldstein B (2012). Triggering a cell shape change by exploiting preexisting actomyosin contractions. Science 335, 1232–1235.
Segal D, Zaritsky A, Schejter ED, Shilo B-Z (2018). Feedback inhibition of actin on Rho mediates content release from large secretory vesicles. J Cell Biol 217, 1815–1826.
Sailer A, Anneken A, Li Y, Lee S, Munro E (2015). Dynamic opposition of clustered proteins stabilizes cortical polarity in the *C. elegans* zygote. Dev Cell 35, 131–142.
Smith MA, Blankman E, Gardel ML, Luettjohann L, Waterman CM, Beckerle MC (2010). A zyxin-mediated mechanism for actin stress fiber maintenance and repair. Dev Cell 19, 365–376.
Solon J, Kaya-Copur A, Colombelli J, Brunner D (2009). Pulsed forces timed by a ratchet-like mechanism drive directed tissue movement during dorsal closure. Cell 137, 1331–1342.
Stephenson RE, Higashi T, Erofeev IS, Arnold TR, Leda M, Goryachev AB, Miller AL (2019). Rho flares repair local tight junction leaks. Dev Cell 48, 445–459.e5.
Strogatz SH (2019). Nonlinear Dynamics and Chaos: With Applications to Physics, Biology, Chemistry, and Engineering, Boca Raton, FL: CRC Press.
Sun X, Phua DYZ, Axiotakis L, Smith MA, Blankman E, Gong R, Cail RC, Reyes SE, Beckerle MC, Waterman CM, *et al*. (2020). Mechanosensing through direct binding of tensed F-actin by LIM domains. Dev Cell 55, 468–482.e7.
Sutherland A, Lesko A (2020). Pulsed actomyosin contractions in morphogenesis. F1000Research 9.
Tian D, Diao M, Jiang Y, Sun L, Zhang Y, Chen Z, Huang S, Ou G (2015). Anillin regulates neuronal migration and neurite growth by linking RhoG to the actin cytoskeleton. Curr Biol 25, 1135–1145.
Timmons L, Court DL, Fire A (2001). Ingestion of bacterially expressed dsRNAs can produce specific and potent genetic interference in *Caenorhabditis elegans*. Gene 263, 103–112.
Tse YC, Piekny A, Glotzer M (2011). Anillin promotes astral microtubule-directed cortical myosin polarization. Mol Biol Cell 22, 3165–3175.
Watanabe S, Okawa K, Miki T, Sakamoto S, Morinaga T, Segawa K, Arakawa T, Kinoshita M, Ishizaki T, Narumiya S (2010). Rho and anillin-dependent control of mDia2 localization and function in cytokinesis. Mol Biol Cell 21, 3193–3204.
Winkelman JD, Anderson CA, Suarez C, Kovar DR, Gardel ML (2020). Evolutionarily diverse LIM domain-containing proteins bind stressed actin filaments through a conserved mechanism. Proc Natl Acad Sci USA 117, 25532–25542.
Xiong D, Xiao S, Guo S, Lin Q, Nakatsu F, Wu M (2016). Frequency and amplitude control of cortical oscillations by phosphoinositide waves. Nat Chem Biol 12, 159–166.
Zhao P, Teng X, Tantirimudalige SN, Nishikawa M, Wohland T, Toyama Y, Motegi F (2019). Aurora-A breaks symmetry in contractile actomyosin networks independently of its role in centrosome maturation. Dev Cell 48, 631–645.e6.